



Contents lists available at SciVerse ScienceDirect

Ocean Modelling

journal homepage: www.elsevier.com/locate/ocemod

Limiters for spectral propagation velocities in SWAN

J.C. Dietrich^{a,*}, M. Zijlema^b, P.-E. Allier^{a,1}, L.H. Holthuijsen^b, N. Booij^b, J.D. Meixner^a, J.K. Proft^a, C.N. Dawson^a, C.J. Bender^c, A. Naimaster^c, J.M. Smith^d, J.J. Westerink^e^a Institute for Computational Engineering and Sciences, University of Texas at Austin, United States^b Faculty of Civil Engineering and Geosciences, Delft University of Technology, The Netherlands^c Taylor Engineering, Jacksonville, FL, United States^d Coastal and Hydraulics Laboratory, US Army Corps of Engineers, Vicksburg, MS, United States^e Department of Civil and Environmental Engineering and Earth Sciences, University of Notre Dame, United States

ARTICLE INFO

Article history:

Available online xxx

Keywords:

Wave-current interaction

Refraction

SWAN

Numerical accuracy

ABSTRACT

As phase-averaged spectral wave models continue to grow in sophistication, they are applied more frequently throughout the ocean, from the generation of waves in deep water to their dissipation in the nearshore. Mesh spacings are varied within the computational domain, either through the use of nested, structured meshes or a single, unstructured mesh. This approach is economical, but it can cause accuracy errors in regions where the input parameters are under-resolved. For instance, in regions with a coarse representation of bathymetry, refraction can focus excessive wave energy at a single mesh vertex, causing the computed solution to become non-physical. Limiters based on the Courant–Friedrichs–Lewy (CFL) criteria are proposed for the spectral propagation (refraction and frequency shifting) velocities in SWAN. These limiters are not required for model stability, but they improve accuracy by reducing local errors that would otherwise spread throughout the computational domain. As demonstrated on test cases in deep and shallow water, these limiters prevent the excessive directional turning and frequency shifting of wave energy and control the largest errors in under-resolved regions.

© 2012 Elsevier Ltd. All rights reserved.

1. Motivation

Wind-generated ocean waves are impacted by variability in ambient currents and depths. The statistical properties of the waves, such as their significant heights and peak periods, are modulated by directional turning (refraction) and (Doppler-like) frequency shifting. On a local scale, these phenomena are pronounced over extended tidal flats with shoals and channels or near oceanic islands with shores sloping to great depths over a short distance. On a larger scale, current-induced refraction and frequency shifting occur in oceanic currents such as the Gulf Stream. The proper representation of these processes is a critical component of wave hindcasting and forecasting.

It is inefficient for computational models to resolve the phases of individual waves on large domains, especially when they are extended to shelf and oceanic scales. Instead, wave generation models consider a phase-averaged, statistical description of the wave field, in which the wave energy is conserved. In the presence of ambient currents, the conserved quantity becomes the wave action, or the ratio of energy to relative frequency (Whitham, 1974;

Phillips, 1977; Mei, 1983). Several operational wave models have been developed to conserve wave action, notably WAM (WAMDI Group, 1988; Komen et al., 1994), WaveWatch III (Tolman, 2009), SWAN (Booij et al., 1999; Ris et al., 1999), STWAVE (Smith et al., 2001) and the WWM (Hsu et al., 2005; Roland, 2009).

Most operational models now include the necessary parameterizations to describe the entire evolution of the wave field from generation through transformation to dissipation. Thus, as these models mature, they are applied throughout the ocean. Models that were applicable traditionally in deep water are now extended to the coastline and beyond, e.g., the application of WAM to Liverpool Bay (Brown, 2010) and the Orkney Islands (Bertotti and Cavaleri, 2012), both in the United Kingdom. And models that were applicable traditionally in the nearshore are now extended to the shelf break and beyond, e.g., the application of SWAN to storm hindcasts in the Western Pacific (Babanin et al., 2011). Further advances in computing power have also enhanced the coupling of these spectral wave models to circulation models (Kim and Yamashita, 2008; Bunya et al., 2010; Bennis et al., 2011; Brown et al., 2011; Dietrich et al., 2011a).

To propagate waves from deep to shallow water, spectral wind-wave models have varied mesh spacings within the computational domain through the nesting of multiple structured meshes. The recent extension to unstructured meshes has allowed resolution to

* Corresponding author. Tel.: +1 512 471 5845.

E-mail address: dietrich@ices.utexas.edu (J.C. Dietrich).¹ Current address: Ecole Normale Supérieure de Cachan, France.

vary over several orders of magnitude within a single mesh (Hsu et al., 2005; Qi et al., 2009; Zijlema, 2010). These meshes (either nested-structured or single-unstructured) allow sufficient resolution within the region of interest, but not universally, as the mesh spacings are increased in the far-field to reduce the computational cost. This tendency is perhaps magnified in the case of unstructured meshes constructed with high levels of resolution along a specific stretch of coastline, but relatively lower levels of resolution along distant coasts or islands. The resolution may thus become coarser than in a corresponding structured mesh.

In any numerical model, accuracy errors occur where the mesh spacings are insufficient to resolve gradients in the input parameters or the computed solution. For instance, when the refraction process is under-resolved in a wave model, energy can become focused unrealistically at a single mesh vertex, causing the significant wave heights to become non-physical. The optimal solution to correct these errors would seem to be to increase the geographic and/or spectral resolution so that all of the physical processes are resolved sufficiently throughout the entire domain. However, it is not always economical or feasible to increase resolution far from the region of interest. Another possible solution is to enable selectively the physical processes. For example, the authors have employed the unstructured-mesh version of SWAN in several recent hurricane validation studies, with wave refraction enabled within the northern Gulf of Mexico but disabled in the Caribbean Sea and the Atlantic Ocean (Dietrich et al., 2011a,b, 2012).

A more robust solution is limiting of the spectral propagation velocities, especially the directional turning rate, based on the Courant–Friedrichs–Lewy (CFL) parameter. In models with explicit solution schemes, this parameter can be used to select an appropriate time step, or to limit the refraction to prevent errors when using larger time steps. For example, in WaveWatch III, propagation in θ -space is limited so that the CFL parameter does not exceed a default value of 0.7 (Tolman, 2009). This limiting allows WaveWatch III to propagate long waves in shallow water without the need for extremely small time steps, by effectively reducing the bottom slope. Limiting is not required for stability in models with implicit solution schemes, such as SWAN, but it may become necessary for accuracy reasons. Previous efforts to address this problem in SWAN have focused on a similar reduction in the bottom slope or an alternative formulation of the turning rate in terms of the wave number. These alternative treatments are available to SWAN users, but they are not robust in all applications.

We propose CFL-based limiters for refraction and for frequency shifting in the spectral propagation velocities in SWAN. These limiters are evaluated for idealized test cases and realistic applications, in both deep and shallow water. In under-resolved regions, the largest errors are removed when the turning rate is limited. Non-physical significant wave heights of 150 m or larger are removed in deep water, while non-physical peak periods of 31 s (corresponding to the lowest-resolved frequency bin) are removed in the nearshore. The proper selection of the limiting CFL parameter is problem-dependent, but guidance is provided for a variety of meshes and applications. It is emphasized that these limiters cannot eliminate the inaccuracies that are caused by insufficient resolution, but they can control the largest accuracy errors in under-resolved regions and prevent them from spreading throughout the computational domain.

2. Methods

2.1. Simulating waves nearshore (SWAN)

SWAN represents the wave field as a phase-averaged spectrum (Booij et al., 1999; Ris et al., 1999). The wave action density

$N(t, \lambda, \varphi, \sigma, \theta)$ evolves in time (t), geographic space (with longitudes λ and latitudes φ) and spectral space (with relative frequencies σ and directions θ), as governed by the action balance equation:

$$\begin{aligned} \frac{\partial N}{\partial t} + \frac{\partial}{\partial \lambda} [(c_{g,\lambda} + u_\lambda)N] + \cos^{-1} \varphi \frac{\partial}{\partial \varphi} [(c_{g,\varphi} + u_\varphi)N \cos \varphi] \\ + \frac{\partial}{\partial \theta} [c_\theta N] + \frac{\partial}{\partial \sigma} [c_\sigma N] = \frac{S_{tot}}{\sigma} \end{aligned} \quad (1)$$

where $\vec{c}_g = (c_{g,\lambda}, c_{g,\varphi})$ is the group velocity, $\vec{u} = (u_\lambda, u_\varphi)$ is the ambient current, and c_θ and c_σ are the propagation velocities in the θ - and σ -spaces. The velocity c_θ represents bottom- and current-induced refraction, optionally supplemented with a diffraction approximation. The velocity c_σ represents Doppler-type frequency shifting due to currents and time-varying depths. Diffraction would be handled separately (Holthuijsen et al., 2003), but is not included in the present simulations.

The propagation velocities in spectral space are derived in the Appendix A, and they are functions of the total water depth $H = h + \zeta$, where h is the bathymetric depth measured downward from the mean water level and ζ is the water surface deviation from the mean, and the ambient currents $\vec{u} = (u_\lambda, u_\varphi)$. The quantities ζ and \vec{u} are provided via the ‘tight’ coupling of SWAN with the Advanced CIRCulation (ADCIRC) model (Kolar et al., 1994; Luettich and Westerink, 2004; Dawson et al., 2006; Westerink and Coauthors, 2008). The tightly-coupled SWAN+ADCIRC model allows waves and circulation to be simulated on the same unstructured mesh and by the same executable program, so that information can be passed between models via local cache or memory, without the need for interpolation between heterogeneous meshes (Dietrich et al., 2011a, 2012).

The source terms S_{tot} represent wave growth by wind; energy lost due to whitecapping, depth-induced breaking and bottom friction; and energy exchanged between spectral components due to nonlinear effects in deep and shallow water. Herein, wind input is based on the formulation from Cavaleri and Malanotte-Rizzoli (1981) and Snyder et al. (1981), whitecapping is applied via the expression of Komen et al. (1984) as modified by Rogers et al. (2003), and nonlinear quadruplet interactions are computed using the discrete interaction approximation of Hasselmann et al. (1985). In shallow water, bottom friction is parameterized via the conversion of spatially-variable Manning’s n values into roughness lengths (Bretschneider et al., 1986; Madsen et al., 1988; Dietrich et al., 2011b), while depth-induced breaking is computed with a spectral version of the model due to Battjes and Janssen (1978) with the breaking index $\gamma = 0.73$. Nonlinear triad interactions are neglected. These source term parameterizations are similar to recent studies using SWAN+ADCIRC, e.g. Dietrich et al., 2011b.

SWAN discretizes the action balance equation via the finite difference method. A third-order upwind scheme is applied to the advection terms in geographic space (Stelling and Leendertse, 1992), with a diffusive correction for the garden-sprinkler effect (Booij and Holthuijsen, 1987). In spectral space, a hybrid scheme between central and upwind differencing is applied. A Gauss–Seidel iterative technique is employed to update the action densities in geographic space, by ordering the vertices and then sweeping through them in opposite directions. At each geographic vertex, the solution is updated within the sector of spectral space corresponding to the sweeping direction (Booij et al., 1999; Zijlema and van, 2005). This update requires the iterative solution of a pentadiagonal matrix system via the strongly implicit procedure (Ferziger and Peric, 1999). The source terms are linearized and included in this matrix system. The unstructured-mesh version of SWAN uses a similar sweeping technique, and the solution in spectral space is identical in the two versions (Zijlema, 2010). This solution method is implicit and thus unconditionally stable.

It is interesting to note that the above-described approach is equivalent to the application of the well-known semi-Lagrangian approximation, and, in fact, is nothing more than the method of characteristics. Consider the material derivative of the action density, but now in Cartesian space:

$$\frac{dN}{dt} \equiv \frac{\partial N}{\partial t} + c_x \frac{\partial N}{\partial x} + c_y \frac{\partial N}{\partial y} \quad (2)$$

where $(c_x, c_y) = \vec{c}_g + \vec{u}$ is the propagation velocity vector. This material derivative indicates that the time rate of change is computed along the wave characteristics:

$$\frac{dx}{dt} = c_x, \quad \frac{dy}{dt} = c_y.$$

For the purpose of illustration, the spatial derivatives are replaced by first-order upwind differences on a structured mesh. If c_x and c_y are positive during the first sweep (Fig. 1), then Eq. (2) can be approximated as:

$$\frac{N_{ij}^{n+1} - N_{ij}^n}{\Delta t} + c_x \frac{N_{ij}^{n+1} - N_{i-1,j}^{n+1}}{\Delta x} + c_y \frac{N_{ij}^{n+1} - N_{i,j-1}^{n+1}}{\Delta y}$$

where Δt is the time step, and Δx and Δy are the mesh spacings in the x - and y -directions, respectively. Note that the time integration is based on the first-order implicit Euler scheme. This approximation can be rewritten as:

$$\left(\frac{1}{\Delta t} + \frac{c_x}{\Delta x} + \frac{c_y}{\Delta y} \right) N_{ij}^{n+1} - \frac{1}{\Delta t} N_{ij}^n - \frac{c_x}{\Delta x} N_{i-1,j}^{n+1} - \frac{c_y}{\Delta y} N_{i,j-1}^{n+1}$$

which can be interpreted as an approximation of the material derivative in Eq. (2), as follows:

$$\frac{N_{ij}^{n+1} - N_{i^*,j^*}^n}{\Delta T}$$

with:

$$\frac{1}{\Delta T} = \frac{1}{\Delta t} + \frac{c_x}{\Delta x} + \frac{c_y}{\Delta y}$$

and:

$$i^* = i - c_x \Delta t, \quad j^* = j - c_y \Delta t, \quad c_x \equiv \frac{|c_x| \Delta t}{\Delta x}, \quad c_y \equiv \frac{|c_y| \Delta t}{\Delta y}.$$

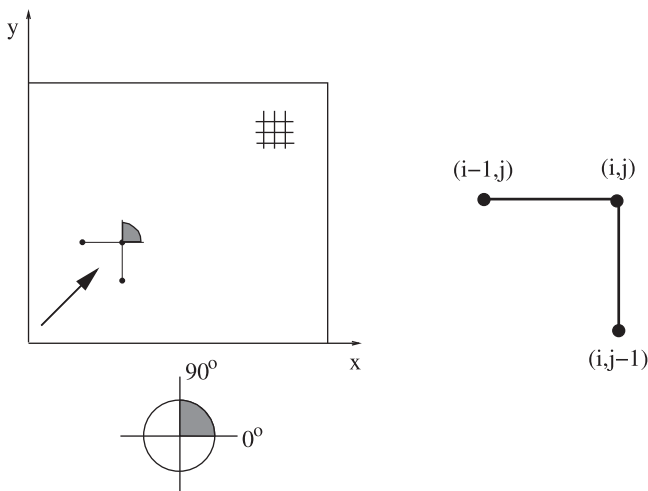


Fig. 1. Numerical scheme for wave propagation in Cartesian space on a structured mesh, with: (left) the first quadrant for which the waves are propagated, and (right) the computational stencil.

Note that the CFL parameters, C_x and C_y , are not integers, and therefore the point (i^*, j^*) is not a mesh vertex. However, this point lies on the wave characteristic. The quantity N_{i^*,j^*}^n can be interpreted as the value of N at time t^n in (i^*, j^*) , which is advected in (i, j) in a lapsed time Δt . This value is obtained via interpolation of the surrounding values in the (t, x, y) -plane. In this case, there is no restriction on time step Δt because the characteristic lies inside the computational stencil.

2.2. Limiters on spectral propagation velocities

An important assumption made in the above discussion is that c_x and c_y do not vary quickly over a time step while propagating along the characteristic. This assumption is reasonable because the wave characteristics are nearly straight lines (over the time step), as the geographic propagation varies slowly in time. However, this assumption may not hold for spectral propagation. Wave refraction due to gradients in bottom slope and ambient currents can vary quickly in time. Often the associated time scale is much shorter than the time step used in a numerical simulation. In one time or distance step, the energy can travel over more than the directional interval of one sweep (which, in the absence of currents, is 90° on a structured mesh, see Fig. 1). This behavior is more likely to occur when the bathymetry is resolved poorly by the mesh, as will be shown later. A similar effect may be observed in the frequencies when waves enter an opposing current. If the current gradient is large, then energy may be forced to shift over more than one frequency bin in the discretized spectrum as the waves travel over only on geographic element.

Thus, for physical consistency, the waves must be prevented from crossing the boundaries of a quadrant in spectral space. As noted previously, unpublished efforts to address excessive directional turning in SWAN have focused on limiting the bottom slope, i.e., through the selection of β such that:

$$H_* - H_{ij} \leq \beta H_{ij}$$

where H_{ij} is the depth at the vertex of interest, and H_* is the depth at a neighboring vertex. This treatment is similar conceptually to that used by WaveWatch III (Tolman, 2009) in that the effective reduction in bottom slope allows long waves to propagate in shallow water. Another effort focused on replacing the treatment of the turning rate c_θ with an alternative formulation in terms of the wave number (Rogers et al., 2007). However, practical experience with these limiters has shown that they are not robust, especially when the gradients in bottom topography and/or ambient currents become large. The corresponding problem of excessive frequency shifting has not been addressed previously and will be discussed in this work.

The approach herein limits the total directional turn or total frequency shift to about one spectral bin as the waves propagate over a geographic element, not for reasons of stability but for reasons of accuracy. The CFL parameters based on ΔT , $\Delta\theta$ (directional bin) and $\Delta\sigma$ (frequency bin) for directional turning and frequency shifting are as follows:

$$C_\theta \equiv \frac{|c_\theta| \Delta T}{\Delta\theta} \leq \alpha_\theta \quad (3)$$

and:

$$C_\sigma \equiv \frac{|c_\sigma| \Delta T}{\Delta\sigma} \leq \alpha_\sigma \quad (4)$$

with c_θ the turning rate and c_σ the frequency shifting (as discussed in the Appendix A), and $\alpha_\theta, \alpha_\sigma$ the maximum CFL parameters defined by the user. Note that Eqs. (3), (4) are not required for the stability of the method, but rather they contribute to remove the largest accuracy errors in under-resolved regions. Thus, it is not re-

quired to select $\alpha_\theta \leq 1$ and $\alpha_\sigma \leq 1$ because of the implicit solution in SWAN.

For instance, in a large-scale application with a desired time step, the user may apply coarsely-resolved, nested meshes or a single unstructured mesh with varying resolution. Both the mesh spacings and the time step may be too large to represent the wave refraction process. The value of c_θ in the shallowest mesh vertex may become too large due to gradients in bottom slopes over a mesh spacing, so that wave energy will change over multiple directional bins or even the directional sector. Limitations would then be:

$$|c_\theta| < \alpha_\theta \Delta\theta \left(\frac{1}{\Delta t} + \frac{|c_x|}{\Delta x} + \frac{|c_y|}{\Delta y} \right)$$

and:

$$|c_\sigma| < \alpha_\sigma \Delta\sigma \left(\frac{1}{\Delta t} + \frac{|c_x|}{\Delta x} + \frac{|c_y|}{\Delta y} \right).$$

The time step Δt is neglected in stationary conditions. Often the desired time step (with typical values of 10 min or larger) is such that the term $1/\Delta t$ can also be neglected in non-stationary conditions, leading to limitations that are slightly more restrictive, and thus provide a safety margin in the CFL parameters:

$$|c_\theta| < \alpha_\theta \Delta\theta \left(\frac{|c_x|}{\Delta x} + \frac{|c_y|}{\Delta y} \right) \tag{5}$$

and:

$$|c_\sigma| < \alpha_\sigma \Delta\sigma \left(\frac{|c_x|}{\Delta x} + \frac{|c_y|}{\Delta y} \right) \tag{6}$$

Similar expressions can also be written in geographic (λ, φ) space. The proper selection of α_θ and α_σ in Eqs. (5), (6) will limit the spectral propagation velocities, and thus prevent wave energy from turning and/or shifting excessively during a single time step. These limiters are not activated automatically by SWAN, but rather they are enabled at the discretion of the user. The results presented here support a selection in the range of 0.25 to 0.5, but the user may specify any values to balance control of the non-physical behavior and energy propagation.

It is noted that the user's ability to select the values of the limiters is an advancement over previous efforts. However, it must be stressed that these limitations are a survival measure and may affect locally the solution. For instance, when the turning rate is limited and the largest accuracy errors are removed, the wave energy is still allowed to propagate to other regions. In some cases, this propagation behavior may be desirable. For example, in the circular-shoal and elliptic-mound test cases that follow, the limiters allow wave energy to propagate past submerged features in ways that are similar to the propagation behavior on meshes with sufficient levels of resolution. But it is possible to envision scenarios in which, by preventing directional turning and/or frequency shifting, wave energy would be sent into regions where it would not travel naturally. In those cases, the computed solution can only be improved by resolving the physical processes through careful discretization in time, geographic and spectral space.

3. Results

In the following sections, the limiters are evaluated for applications in deep and shallow water. Unless otherwise noted, these simulations utilize natural bathymetric gradients, ambient currents, and wave-induced currents and set-up. The SWAN time step and coupling interval are 600 s. The solutions on unstructured meshes utilize the default SWAN convergence criteria. SWAN iterates until 95 percent of the vertices in the global domain have con-

verged, to a maximum of 20 iterations. Refraction and frequency shifting are allowed everywhere, unless limited as noted.

3.1. Circular shoal

Before evaluating the limiters in test cases including realistic bathymetry, source terms and ambient currents, they are evaluated first in an idealized test case in which waves are refracted over a near-circular shoal (Fig. 2); this case was designed to match a similar feature in the southern California Bight (Rogers et al., 2007). For this idealized case, the source terms S_{tot} are set to zero in Eq. (1), and the ambient and wave-induced currents and set-up are neglected. At the north, west and south boundaries, a directional JONSWAP spectrum ($\gamma = 3$) is imposed with $H_s = 0.5$ m, $T_p = 15.2$ s, a mean direction of -65° (measured clockwise from geographic north), and the cosine power $m = 14$ (i.e., directional spreading is 15°).

Two structured meshes are employed: a fine rectangular mesh with $\Delta x = \Delta y \approx 300$ m, and a coarse rectangular mesh with $\Delta x = \Delta y \approx 3000$ m (Fig. 2). The spectral domain is discretized with 33 frequency bins that are distributed logarithmically from 0.05–1 Hz, as well as constant directional bins with $\Delta\theta = 10^\circ$. The

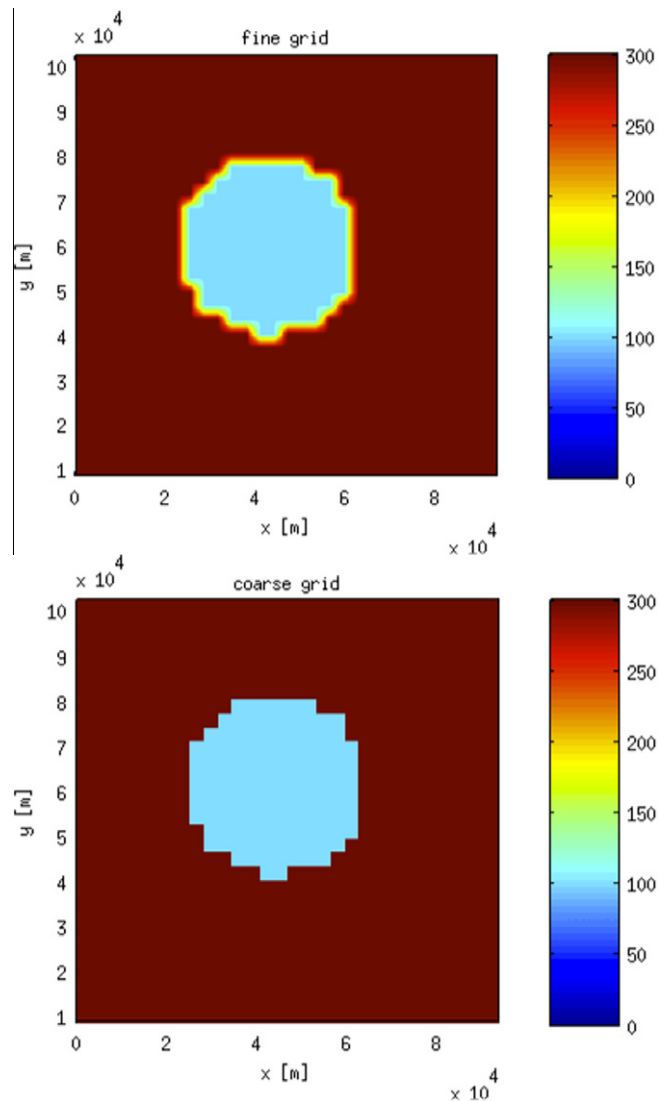


Fig. 2. Bathymetry (m) of the near-circular shoal test case, with fine (top) and coarse (bottom) mesh resolution.

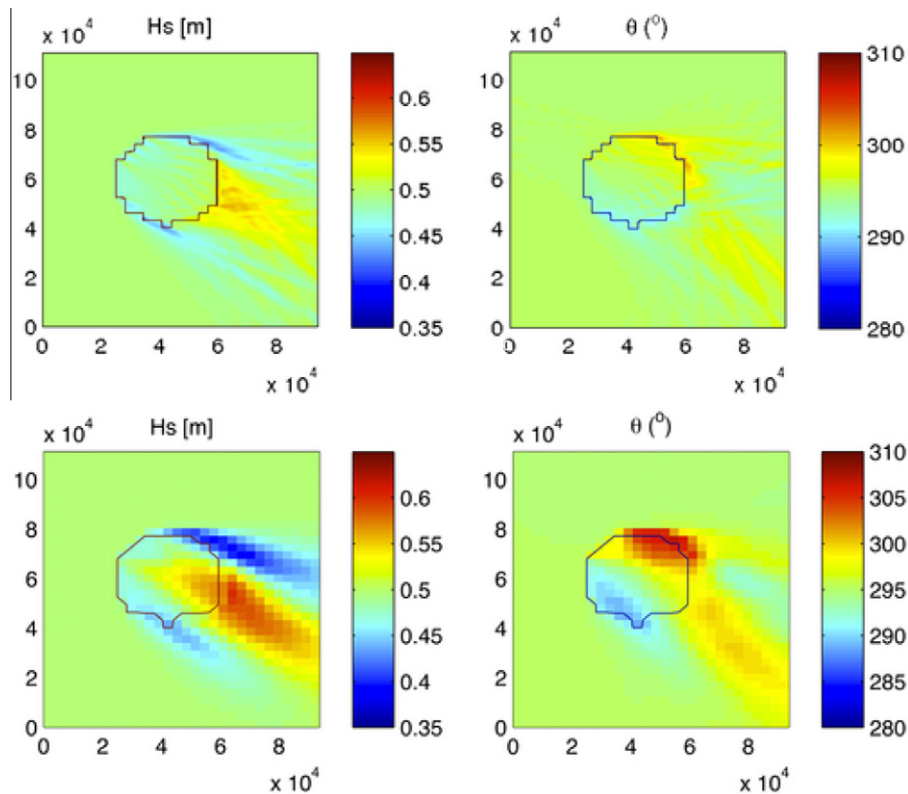


Fig. 3. Contours of significant wave heights (m) and mean wave directions ($^{\circ}$), without the c_{θ} -limiter, on the fine (top row) and coarse (bottom row) mesh resolutions.

simulation is performed first on both meshes without a limiter on c_{θ} ; Fig. 3 depicts the significant wave heights and mean wave directions throughout the domain. Note the waves are refracted strongly behind the shoal on the finely-resolved mesh. When the simulation is repeated on the coarse mesh, the waves refract prematurely on the shoal.

When the turning rate is limited with $\alpha_{\theta} = 0.35$ (Fig. 4), the premature refraction is eliminated on the coarse mesh and the solution is qualitatively similar to the unlimited solution on the fine mesh. (Note that this is the largest value of α_{θ} for which the coarse-mesh solution is a good approximation of the fine-mesh solution.) To demonstrate that the turning rate limiter does not affect adversely the solution on the fine mesh, the limiter is applied. The solutions on the fine mesh are identical, regardless of whether the turning rate is unlimited or limited, suggesting that the fine mesh resolution is sufficient to capture the refraction process. However, it is possible to envision scenarios in which the limiter would affect the solution on a fine mesh, especially if the user selects a value that conflicts with the existing CFL conditions.

3.2. Submerged mounds in deep water

Submerged mounds are prevalent within the Caribbean Sea and the southern Atlantic Ocean, as well as other regions of the world, where the islands and surrounding bathymetry can have steep gradients. These gradients are difficult to represent in computational meshes without high levels of horizontal resolution, but this resolution can be inefficient when the focus is on larger-scale processes in these basins. For instance, this region may be included in a model domain to allow tides to propagate correctly into the Gulf, or to allow the dissipation of swell that has been generated elsewhere. The mesh resolution must provide an economical representation of the bathymetric variability in this region.

3.2.1. Elliptic mound

An idealized representation of a submerged mound is shown in Fig. 5(a), with conditions selected to be similar to those described in the Katrina hindcast in the following section. This test domain spans 7.5° longitude and 3° latitude, and it contains a submerged mound with a width of 0.2° , a length of 0.6° , and a rotation angle of 45° (so that its major and minor axes are not aligned with lines of constant longitude and latitude). The bathymetric depth is 1000 m but slopes upward to 200 m at the top of the mound. In ADCIRC, a current of 0.1 m s^{-1} is specified from north to south, while in SWAN, an incoming wave is specified at the north boundary with a JONSWAP spectrum characterized by a peak enhancement parameter $\gamma = 3.3$, a significant height $H_s = 10 \text{ m}$, a peak period $T_p = 15 \text{ s}$, a mean direction of 270° (southward), and a directional standard deviation of 30° . The source terms are neglected in SWAN for this test case.

This domain is discretized (Fig. 5(b)) via the application of an unstructured mesh with near-uniform spacing of 0.15° . The mesh is required to position a vertex at the top of the mound (with a bathymetric depth of 200 m), but otherwise the finite elements are generated automatically by the Surface-water modeling solution (SMS, <<http://www.aquaveo.com/sms>>) software. Bathymetry is interpolated linearly from the idealized conditions. The spectral domain is discretized with 30 frequency bins that are distributed logarithmically from 0.031–0.55 Hz, as well as constant directional bins with $\Delta\theta = 2^{\circ}$. (Note that this directional discretization was necessary to replicate the non-physical behavior on this relatively simple test domain.)

The ambient currents are relatively small, with values of 0.1 m s^{-1} slightly north and south of the submerged mound, and a value of 0.2 m s^{-1} above it. The bathymetric gradients are the primary cause of the turning of wave energy in spectral space. When the spectral propagation velocities are unlimited (Fig. 5(c)), the H_s range upward to 195 m over the mound, and they propagate west-

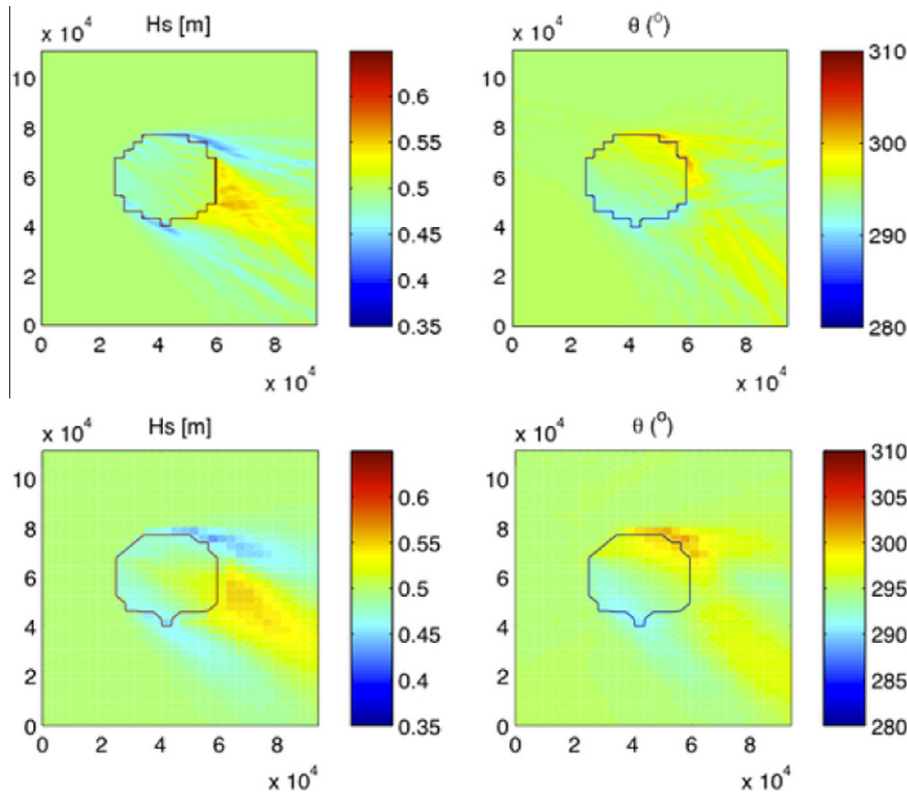


Fig. 4. Contours of significant wave heights (m) and mean wave directions ($^{\circ}$), with c_{θ} limited and $\alpha_{\theta} = 0.35$, on the fine (top row) and coarse (bottom row) mesh resolutions.

ward (and perpendicular to the mean direction that was specified at the northern boundary). This non-physical response is caused by excessive refraction. In Fig. 6(b), the variance densities are shown in spectral space for the geographic vertex above the mound. The excessive refraction pushes wave energy into an extraneous peak, which ranges upward to a maximum of $772 \text{ m}^2/\text{Hz}^{\circ}$ and has a direction of 147° (westward).

The solution improves dramatically when the turning rate c_{θ} is limited via the selection in Eq. 5 of $\alpha_{\theta} = 0.5$ (to match the analysis for the Katrina test case that follows). The variance densities (Fig. 6(c)) have a peak direction of 270° (southward), and their magnitudes are reasonable. The corresponding significant wave heights (Fig. 5(d)) decrease smoothly from the $H_s = 10 \text{ m}$ specified at the northern boundary. The submerged mound does not cause the solution to deteriorate and become non-physical.

A benefit of this test case is that it can be refined in geographic space to provide a ‘true’ solution. The original solution is compared to an unlimited solution on an over-resolved mesh with geographic spacings decreased by a factor of $1/8$, and bathymetry re-interpolated from the idealized conditions. The limited solution on the original mesh (Fig. 6(c)) is nearly identical to the true solution on this over-resolved mesh (Fig. 6(a)). To obtain guidance on the proper selection of α_{θ} , the limiter was varied over several orders of magnitude, and global error norms were computed relative to the true solution on the over-resolved mesh. The root-mean-square (RMS) error was computed as:

$$RMS = \sqrt{\frac{1}{N_p} \sum_{i=1}^{N_p} (P_{i,coarse} - P_{i,fine})^2}$$

and the L_{∞} norm was computed as:

$$L_{\infty} = \max(P_{i,coarse} - P_{i,fine})$$

where N_p is the number of geographic vertices on the original mesh, and P_i are the integrated wave parameters (either H_s or T_p) on the original and fine meshes. The errors with respect to the CFL parameter C_{θ} are shown in Fig. 7. When the turning rate is unlimited, the corresponding CFL parameter is $C_{\theta} = 34$ above the mound, and the H_s errors of $RMS = 27 \text{ m}$ and $L_{\infty} = 180 \text{ m}$ confirm problems with the solution throughout the domain. When $C_{\theta} = \alpha_{\theta} = 2$, the solution is still reasonable, as the H_s errors are decreased to $RMS = 0.02 \text{ m}$ and $L_{\infty} = 0.4 \text{ m}$. The ‘true’ solution on the fine mesh has a maximum $C_{\theta} = 2.5$, which explains the improvement in behavior on the coarse mesh when the limiter is less than that value. The coarse-mesh errors remain constant for smaller limiters, including $\alpha_{\theta} = 0.5$.

3.2.2. Hurricane Katrina (2005) in the Caribbean Sea

Katrina was an especially large and devastating storm, as it reached Category 5 on the Saffir–Simpson scale within the Gulf, and it made landfall in Louisiana and Mississippi as a Category 3 storm. It created waves with significant heights that were measured at 17.5 m within the deeper Gulf, and the 8.8 m storm surge along the Mississippi coastline was the largest ever measured in the United States (Knabb et al., 2005; Ebersole et al., 2007). A wind field for Katrina was developed through the assimilation of measured winds in the inner core by using the National Oceanic and Atmospheric Administration (NOAA) Hurricane Research Division Wind Analysis System (H*WIND) (Powell et al., 1996, 1998) and then blending with Gulf-scale winds using an Interactive Objective Kinematic Analysis (IOKA) system (Cox et al., 1995; Cardone and Cox, 2009). These wind fields have been applied to hindcasts of Katrina in previous studies using ADCIRC and SWAN+ADCIRC (Ebersole et al., 2010; Bunya et al., 2010; Dietrich et al., 2010, 2011a, 2012), with a particular focus on the system’s response in the northern Gulf and within Louisiana, Mississippi and Alabama.

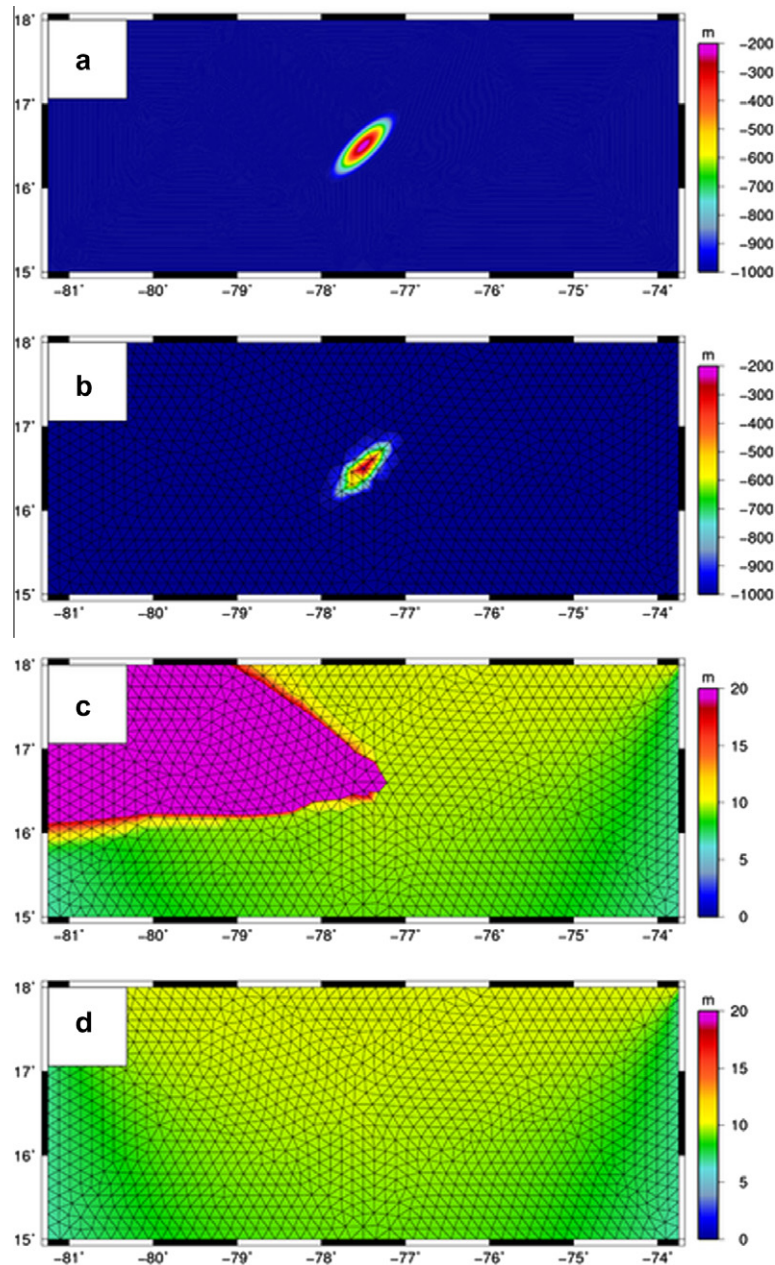


Fig. 5. The submerged mound test domain, with panels of: bathymetry (m) from (a) idealized conditions and (b) as interpolated to the unstructured mesh, and maximum significant wave heights (m) with (c) unlimited propagation velocities and (d) the turning rate limited with $\alpha_0 = 0.5$. In panel (c), the H_s range upward to 195 m.

These studies have led to the assessment of coastal flooding risk and the design of levee protection systems (Ebersole et al., 2007; FEMA, 2009; USACE, 2009).

The focus herein is the SWAN-computed wave behavior in the southern Gulf, the Caribbean Sea and the Atlantic Ocean, i.e., far from the typical region of interest. The Katrina hindcast is simulated on the Eastcoast 2001 (EC2001) unstructured mesh (Fig. 8), which was created during the development of a tidal constituent database (Mukai et al., 2002), and thus its resolution is sufficient to propagate the tidal signal from the specified ocean boundary at the 60°W longitude, across the Atlantic Ocean and Caribbean Sea, and into the resonant Gulf. Mesh spacings range from 20–25 km in the Atlantic Ocean, to 15–20 km in the deeper Gulf, to 5–8 km on the continental shelves, to 1 km or less near southern Louisiana. Recently, higher-resolution meshes for hurricane storm surge have been extended from this mesh, by increasing the reso-

lution within the Gulf to 4–6 km and adding inland coverage (Bunya et al., 2010; Dietrich et al., 2011b). Even in those newer meshes, though, the resolution outside the Gulf has remained the same. The EC2001 mesh contains 492,179 triangular elements.

The Katrina wind fields are applied for a 7-day simulation. The spectral space in SWAN is discretized with 36 directional bins with spacing 10° and 40 frequency bins with logarithmic spacing over the range 0.031–1.42 Hz. The frequencies are discretized logarithmically so that the ratio $\Delta f/f = 0.1$, because the quadruplet nonlinear interactions are computed via the discrete interaction approximation that is tuned to that ratio.

The maximum significant wave heights during the simulation are shown in Fig. 9(a). Along Katrina's track in the Gulf, the wave heights are reasonable and range upward to about 17 m. The largest waves correlate strongly with the strongest winds to the northeast of the track, and these large waves spread throughout the Gulf.

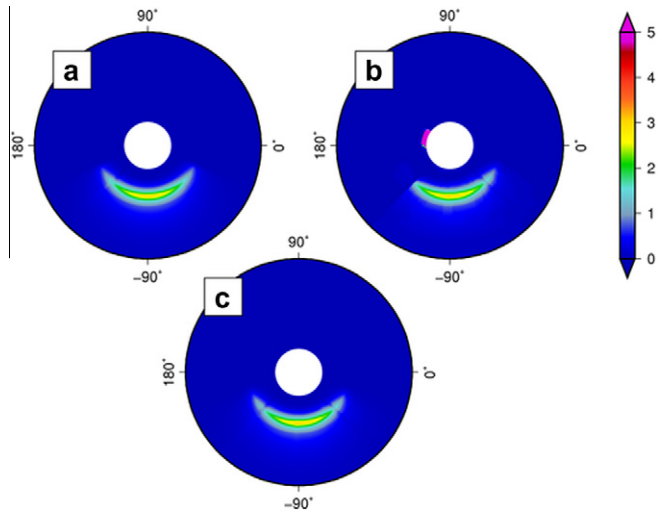


Fig. 6. Variance densities ($\text{m}^2/\text{Hz}^\circ$) in spectral space at the geographic vertex above the submerged mound, with panels corresponding to: (a) unlimited propagation velocities on a mesh with extra resolution in geographic space, (b) unlimited propagation velocities on the original mesh, and (c) the turning rate limited with $\alpha_0 = 0.5$. The frequencies are discretized to 0.55 Hz, but they are shown to a maximum of only 0.15 Hz to highlight the behavior at small frequencies. In panel (b), the variance densities range upward to a maximum of $772 \text{ m}^2/\text{Hz}^\circ$, while in panels (a) and (c), they range to about $3 \text{ m}^2/\text{Hz}^\circ$.

However, away from the track, the computed SWAN solution becomes non-physical. The maximum H_s become as large as 150 m in the southern Gulf, the Caribbean Sea, and into the Atlantic Ocean. This behavior is also experienced outside of the extents of the wind field, where the forced wind velocities are zero.

A closer examination shows the non-physical behavior is caused by the wave refraction reacting unfavorably with the EC2001 mesh bathymetry. Fig. 10 shows an example within the Caribbean Sea. This region lies outside the coverage of the wind forcing, and thus the significant wave heights should be negligible. Fig. 10a shows the most recent bathymetry from the ETOPO1 database (Amante and Eakins, 2009, <<http://www.ngdc.noaa.gov/mgg/global/global.html>>), while Fig. 10(b) shows the EC2001 mesh bathymetry, which was interpolated from an earlier ETOPO5 database with less resolution (Mukai et al., 2002). The mesh bathymetry provides a fair match to the observations, with several submerged mounds in otherwise deep water. The submerged mound in the center of the image is represented by a sole vertex

with a depth of about 240 m, while its neighboring vertices have depths that range from 700–1400 m. The mesh spacings near the mound are about 0.15° . Note that this resolution is coarser than in other hindcasts of Katrina, especially on structured meshes, e.g., the regular 0.1° mesh employed by Wang and Oey (2008).

Waves are generated by the winds within the Gulf and then propagate elsewhere. In this region, the swell approaches the submerged mounds and refracts due to the gradients in bathymetry. This refraction is excessive over the central mound, as the H_s reach a maximum of 83m at that mesh vertex, and then propagate eastward (Fig. 10(c)). The mesh spacings are insufficient to resolve the refraction process in this region. This behavior is repeated farther away from the Gulf, as the mesh spacings grow too large to represent the refraction over the spatially-varying bathymetry of the Caribbean Sea and Atlantic Ocean. As noted earlier, this problem has been addressed previously by disabling the refraction in these regions. Now the turning rate is limited (as in Fig. 9(b)) with $\alpha_0 = 0.5$, which is the largest value for which the non-physical behavior is eliminated. The significant wave heights are near zero outside the extents of the wind field, while the solution near the track remains unchanged.

3.3. Complex bathymetry in the nearshore

Coastal regions often contain complex geometries, steep bathymetric gradients, small-scale islands and channels, etc., which require high levels of resolution. As waves approach these coastal regions, gradients in the bottom topography or ambient currents cause the waves to turn and shift in spectral space. Depending on the local forcing and the representation of geographic features, waves can refract excessively in what would otherwise be considered the ‘high-resolution’ region of a computational mesh.

3.3.1. Coastal ridge

An idealized example of a coastal ridge is shown in Fig. 11(a). This test case is a rectangular 0.1° domain that reproduces the shoaling of waves over a coastal ridge, as in the hindcast of Hugo (1989) in the section below. The depths range from 15 m in the southeast corner of the domain to 0.5 m in the floodplain to the northwest, with the ridge having a height of 1.5 m above sea level. Forcings are selected to simulate an incoming storm surge. In ADCIRC, the water levels are raised by 2 m and a current of 2 m s^{-1} is specified at the south boundary. In SWAN, an incoming wave is specified at the south boundary with a JONSWAP spectrum characterized by a peak enhancement parameter $\gamma = 3.3$, a significant height $H_s = 6 \text{ m}$, a peak period $T_p = 15 \text{ s}$, a mean direction of 90°

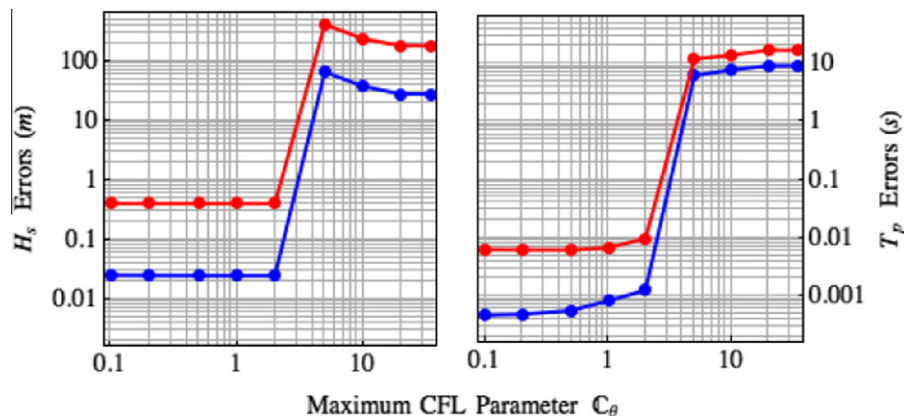


Fig. 7. RMS (blue) and L_∞ (red) errors on the submerged mound test domain, with panels of significant wave heights (left) and peak wave periods (right). Errors are computed relative to an over-resolved solution after one day of simulation. When the turning rate c_θ is unlimited, the CFL parameter $C_\theta = 35$ at the top of the mound (compared with $C_\theta = 2.5$ for the fine-mesh solution). (For interpretation of the references to colour in this figure legend, the reader is referred to the web version of this article.)

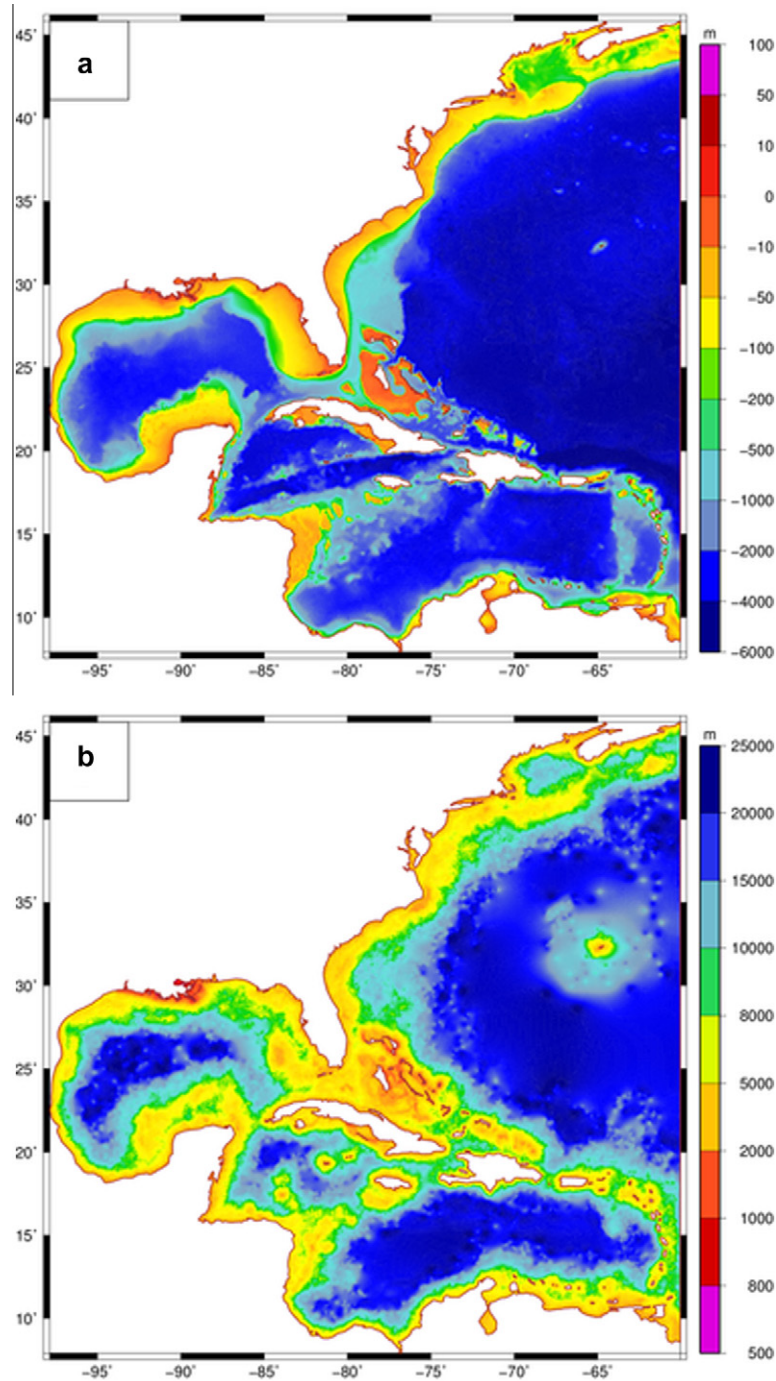


Fig. 8. The EC2001 mesh, with panels of (a) bathymetry (m), and (b) unstructured mesh resolution (m).

(northward), and a directional standard deviation of 30° . A constant, northward wind speed of 30 m s^{-1} is applied to both models.

The domain is discretized on an unstructured mesh with element sizes that vary from about 200 m offshore to about 100 m at the ridge and inland (Fig. 11(b)). A line of vertices is placed along the top of the ridge, but otherwise the finite elements are generated automatically by the SMS software. This mesh contains 15,449 geographic elements. Bathymetry is interpolated linearly from the idealized conditions. The spectral domain is discretized with 30 frequency bins that are distributed logarithmically from 0.031–0.55 Hz, as well as constant directional bins with $\Delta\theta = 1^\circ$. (Note that this directional discretization is small in comparison

to studies on real domains, but it was necessary to replicate the non-physical behavior on this relatively simple test domain.)

A ‘true’ solution was developed by refining this mesh until the solution did not change. This fine mesh contains 3,064,699 geographic elements, and the resolution along the ridge is decreased to about 6 m. When the incoming waves encounter the shallow bathymetry and ultimately move over the ridge, they experience an increase in their peak periods. This behavior is captured on the fine mesh (Fig. 11(c)), where the peak periods increase to about 24 s at the ridge. However, on the original mesh (Fig. 11(d)), the peak periods increase to only about 17–18 s along most of the ridge, indicating that the original resolution is insufficient to

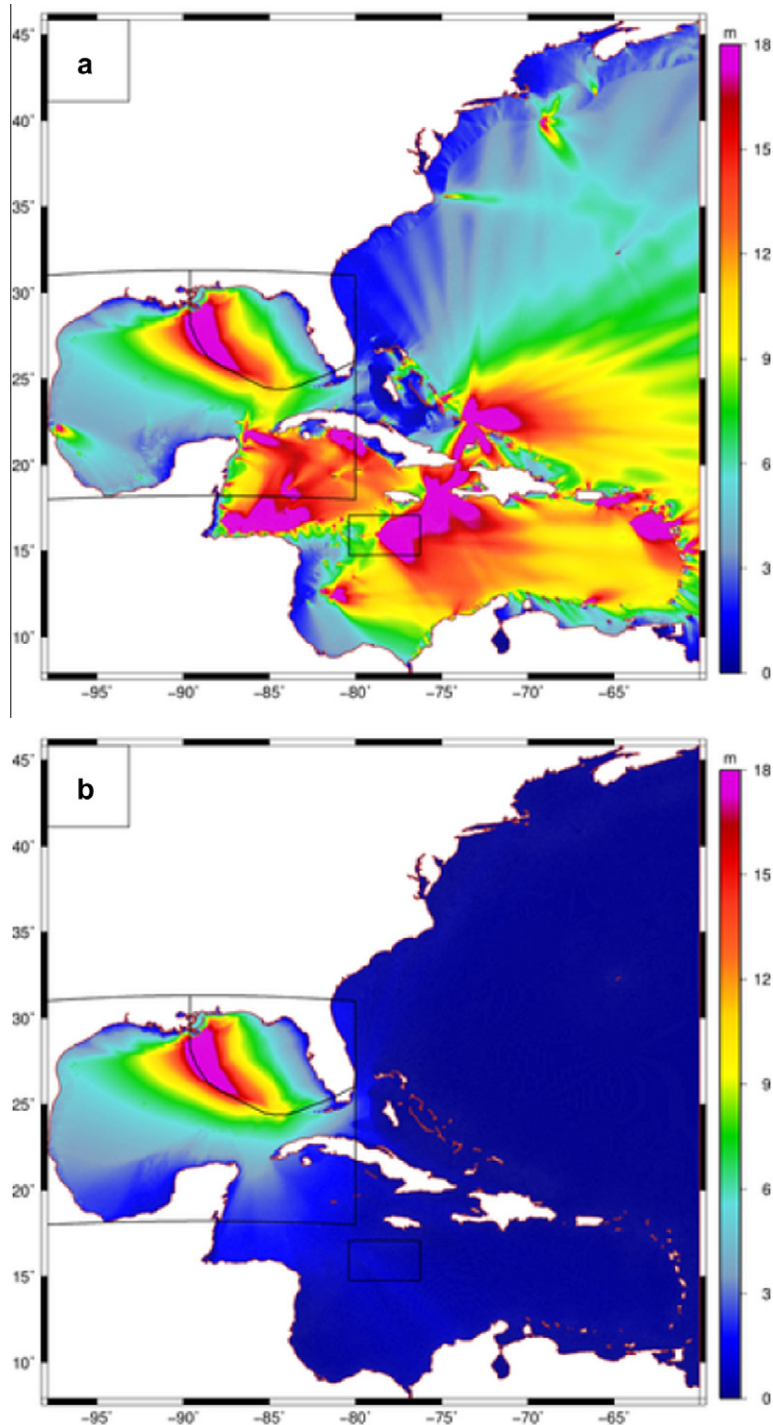


Fig. 9. Maximum significant wave heights (m) during the Katrina hindcast on the EC2001 mesh, with panels of: (a) unlimited spectral propagation velocities, and (b) the turning rate limited with $\alpha_0 = 0.5$. In each panel, the large black box indicates the extents of the wind field, while the small black box in the Caribbean Sea indicates the extents of the zoom shown in Fig. 10. The hurricane track is also indicated.

capture the refraction and peak frequency shifting processes. Instead, at a few vertices along the ridge, the peak periods increase to 31.86 s, the maximum discretized period in this test.

These non-physical peak periods are the result of the turning and shifting of wave energy into smaller discretized frequencies. The variance densities at a geographic vertex near the coastal ridge are shown in Fig. 12. On the fine mesh, the variance densities are smooth and have their largest values at a frequency of about 0.0625 Hz, corresponding to a peak period at this location of about

16 s as the waves begin to shoal over the coastal ridge. Most of this behavior is replicated on the original mesh (Fig. 12(b)), although the solution is not smooth, and an extraneous peak is located eastward and at a smaller frequency. The variance densities are three orders of magnitude larger at this extraneous peak in spectral space. When the refraction and frequency shifting are limited (Figs. 12(c) and (d)), this peak is removed and the computed solution is smooth and reasonable, although the variance densities are asymmetric and centered at a different frequency in comparison to

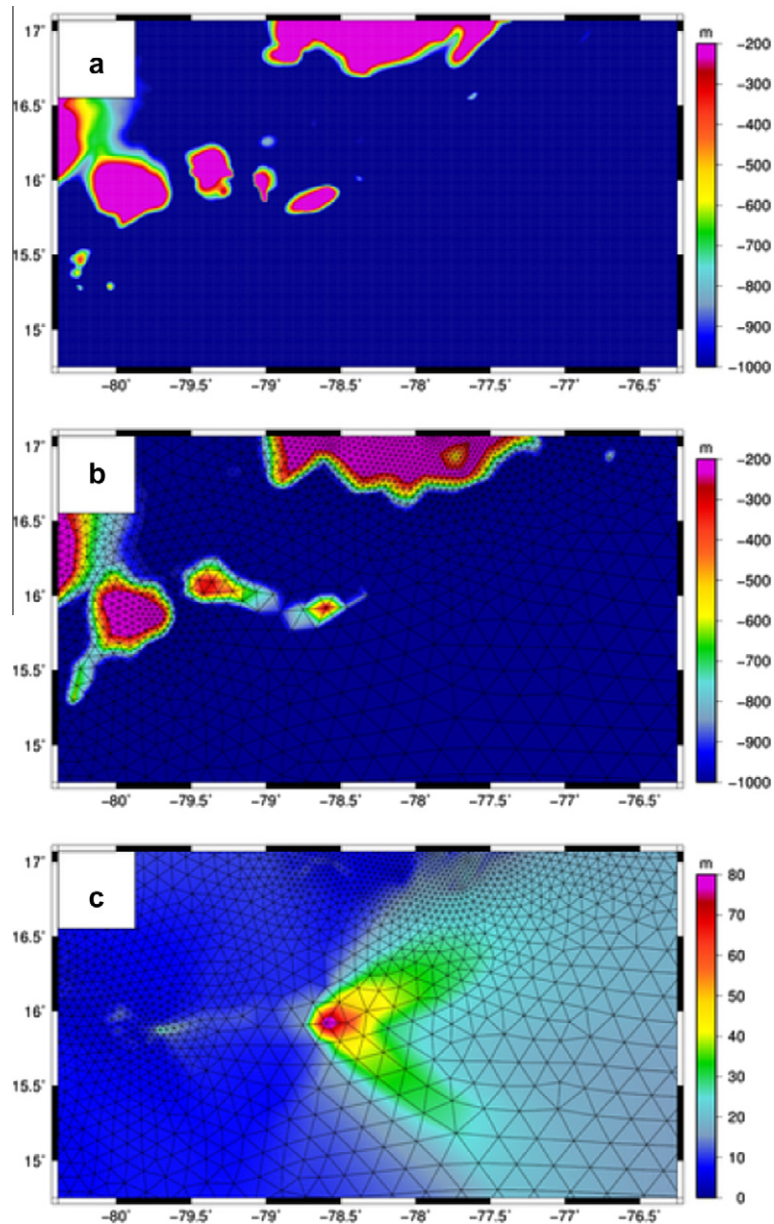


Fig. 10. Details of the Katrina hindcast within the Caribbean Sea, with panels of: (a) bathymetry (m) from the 1 arc-minute ETOPO1 database (Amante and Eakins, 2009); (b) bathymetry (m) in the EC2001 mesh, as interpolated from the ETOPO5 database (Mukai et al., 2002); and (c) maximum significant wave heights (m) with unlimited spectral propagation velocities. When the turning rate is limited with $\alpha_\theta = 0.5$ (not shown), the maximum significant wave heights are negligible throughout this region.

the solution on the fine mesh. This behavior is evident in the peak periods in Figs. 11(e) and (f), as their values of 16–18 s are smaller than the ‘true’ solution with peak periods up to 24 s. The limiters improve the computed solution by preventing excessive refraction and frequency shifting, but they are not a substitute for increased mesh resolution in geographic space.

The depth-limited breaking prevents the significant wave heights from growing to the same large values as in the previous section, and thus the global RMS and L_∞ errors for H_s are constrained (Fig. 13). However, when the velocities are unlimited, the peak periods have an RMS error of about 2 s and an L_∞ error of about 16 s. When the limiters are enabled so that $\alpha_\theta \leq 5$, the solution improves so that the peak periods have an RMS error of about 0.7 s and an L_∞ error of about 7 s. This maximum error is still large, and it reflects the difference in the shoaling over the coastal ridge between the original and fine meshes. When the frequency

shifting is also limited with α_σ , the errors are nearly identical for this test case.

The authors stress that the first choice for improving the accuracy of the computed solution should always be to increase the mesh resolution. However, as this test case demonstrates, that choice is not always economical. In order to remove completely the non-physical behavior caused by the excessive wave refraction, the original mesh must be refined so that the element sizes are about 6 m on the coastal ridge. This refinement increases the overall size of the mesh by a factor of about 200, and the ADCIRC time step must be reduced by a factor of 50 to maintain stability. These refinements have obvious implications on computational cost. If the available computing resources do not support this level of refinement, then the spectral propagation velocity limiters can control economically the largest errors.

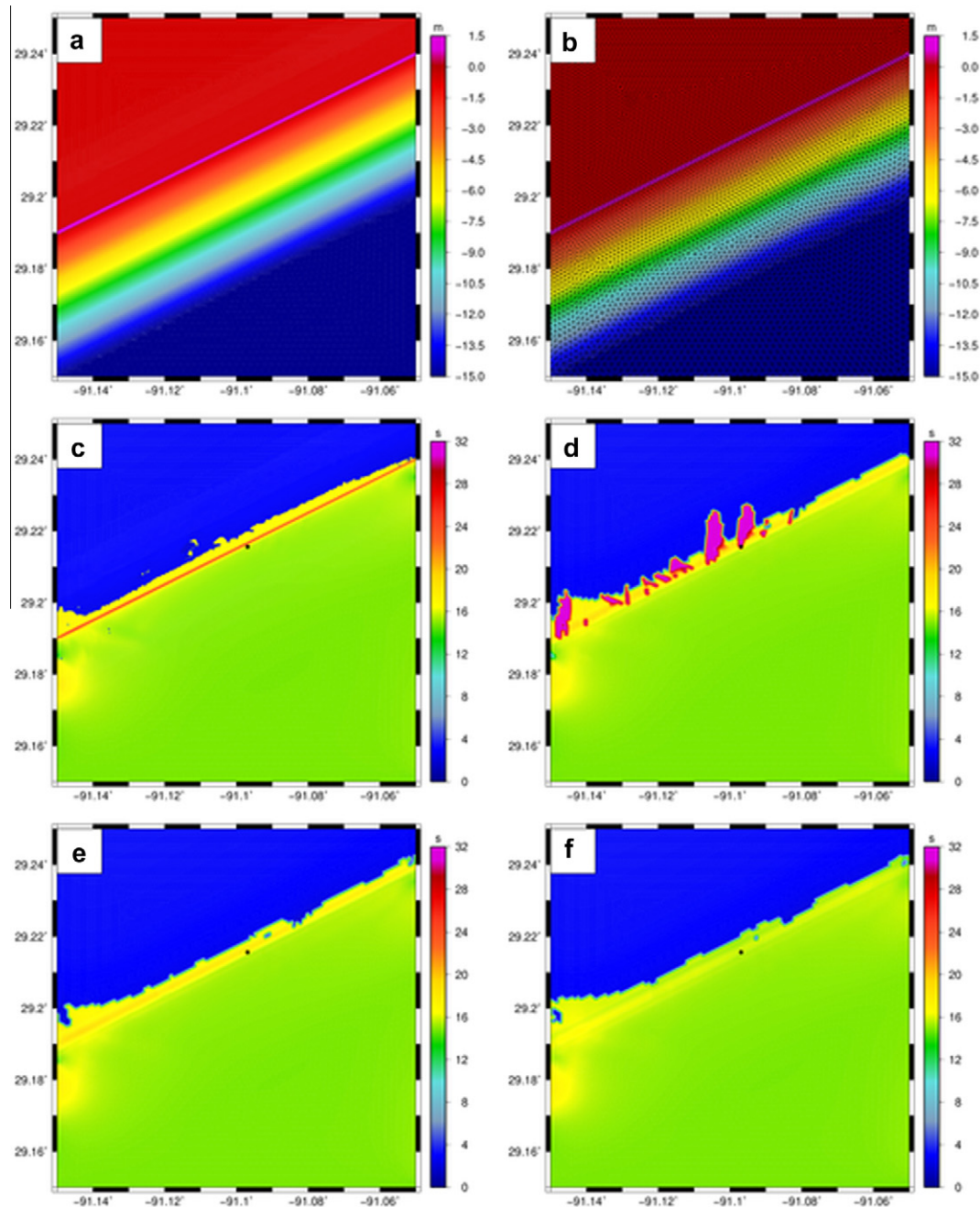


Fig. 11. The shallow-water test domain, with panels of: (a) idealized bathymetry (m), (b) bathymetry (m) interpolated to the unstructured mesh, (c) 'true' peak wave periods (s) on an over-resolved mesh, and peak wave periods (s) on the original mesh with (d) unlimited propagation velocities, (e) the turning rate limited with $\alpha_\theta = 0.25$, and (f) both velocities limited with $\alpha_\theta = \alpha_\sigma = 0.25$. Peak periods are shown after two days of simulation. The black dot in each sub-figure indicates the geographic location where variance densities are shown in Fig. 12.

3.3.2. Hurricane Hugo (1989) in South Carolina

Hugo formed in the Atlantic and reached Category 5 status before tracking near the Caribbean Sea and over Puerto Rico. It strengthened again when it returned to the Atlantic Ocean and made landfall in South Carolina as a Category 4 storm. The eye of the storm passed over Charleston Harbor, causing extensive flooding in the region. Measurements during the storm show waves with significant heights ranging to 8.5 m and peak periods ranging to 16 s as the storm made landfall. The region's response to Hugo has been the subject of previous studies, including several with the structured-mesh version of SWAN (Peng et al., 2006; Xie et al., 2008; Liu and Xie, 2009).

The focus herein is the effect of the limiters on the unstructured-mesh version of SWAN on the continental shelf. The Hugo hindcast is simulated on the South Carolina (SC12) unstructured mesh (Fig. 14). In contrast to the EC2001 mesh described above, a larger percentage of elements in the SC12 mesh are placed within the region of interest, namely the coastline of South Carolina. The mesh spacings are 20 km or larger throughout most of the geographical domain (Fig. 15), but they decrease significantly on the continental shelf and the coastal floodplains. The smallest mesh spacings of about 200 m are located in the region near Charleston Harbor. This mesh was designed for a study of inundation risk, which requires the development of floodplain maps via the statis-

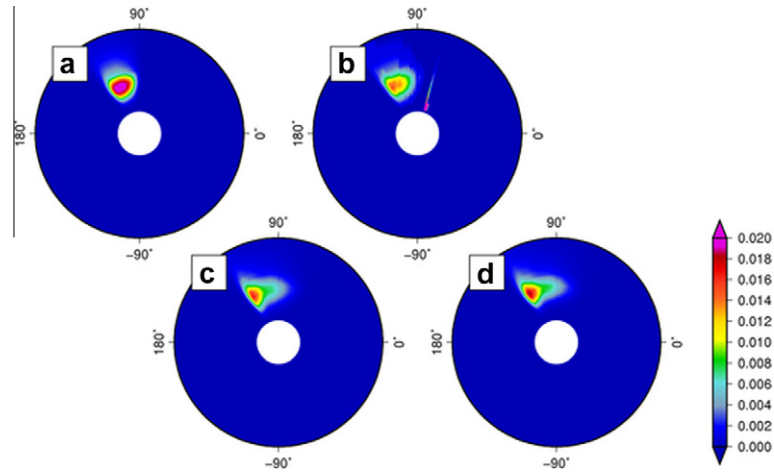


Fig. 12. Variance densities (m^2/Hz^5) in spectral space at the geographic vertex near the coastal ridge, with panels corresponding to: (a) ‘true’ solution on a fine mesh with extra resolution in geographic space, (b) unlimited propagation velocities on the original mesh, (c) the turning rate limited with $\alpha_0 = \alpha_\sigma = 0.25$, and (d) both velocities limited with $\alpha_0 = \alpha_\sigma = 0.25$. The frequencies are discretized to 0.55 Hz, but they are shown to a maximum of only 0.15 Hz to highlight the behavior at low frequencies. In panel (b), the variance densities range upward to a maximum of $12 \text{ m}^2/\text{Hz}^5$, while in panels (c) and (d), they range to about $0.018 \text{ m}^2/\text{Hz}^5$.

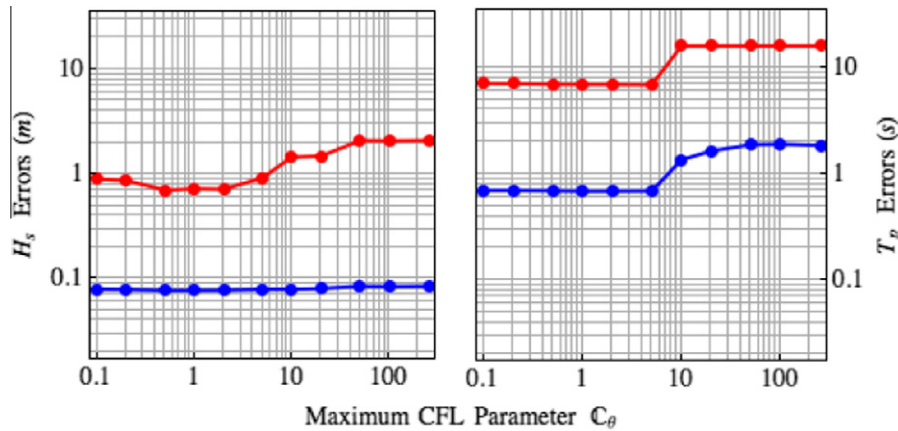


Fig. 13. RMS (blue) and L_∞ (red) errors on the shallow-water test domain, with panels of significant wave heights (left) and peak wave periods (right). Errors are computed relative to an over-resolved solution after two days of simulation. When the turning rate c_θ is unlimited, the CFL parameter $C_\theta = 296$ at the top of the ridge. The errors are nearly identical when both c_θ and c_σ are limited (not shown). (For interpretation of the references to colour in this figure legend, the reader is referred to the web version of this article.)

tical combination of results from simulations of hundreds of theoretical storms, all with varying tracks, intensities, forward speeds, etc. (FEMA, 2012).

The SC12 mesh contains 1,073,925 triangular elements. The Hugo wind fields are applied for an 8-day simulation. The spectral space in SWAN is discretized with 36 directional bins with constant spacing of 10° and 30 frequency bins with logarithmic spacing over the range 0.031–0.547 Hz. The SWAN time step and coupling interval are increased to 20 min. A wind field was developed for Hugo using a similar methodology to that described above for Katrina (Powell et al., 1996, 1998; Cox et al., 1995; Cardone and Cox, 2009; FEMA, 2012).

Hugo was an intense storm, even as it made landfall, and it created large waves that devastated the coastline of central South Carolina. These waves are predicted by the SWAN+ADCIRC hindcast on the SC12 mesh to have significant heights ranging to 20 m near the hurricane’s track, and peak periods ranging to 16–18 s offshore. When the spectral propagation velocities are unlimited (Figs. 16(a) and (b)), the computed SWAN solution is reasonable with respect to the significant wave heights. The bathymetry is

better resolved in the nearshore, and the waves are depth-limited, so there are not any visible inaccuracies caused by excessive refraction. However, starting at the coastline and moving inland, large regions see peak periods of 31.86 s. These long waves are non-physical.

The turning rate must be limited with $\alpha_0 \leq 0.25$ (Fig. 16(d)) to remove the non-physical peak periods throughout much of the region. There are a few exceptions, most notably in the region near Isle of Palms, South Carolina (Fig. 17). The Dewees, Capers and Price Inlets connect the Atlantic Ocean to a complex system of channels, sounds and bays, which require higher levels of mesh resolution than are available due to the project constraints during the development of the SC12 mesh. Energy shifts excessively to focus at the smallest discretized frequency bin, and the peak periods jump to 31.86 s. These incorrect wave periods are evident at the coastal ridge and especially in the back bays. When the frequency shifting is also limited with $\alpha_\sigma = 0.25$, the non-physical peak periods disappear completely within this region (Fig. 17(c)) and throughout the domain (Fig. 16(f)).

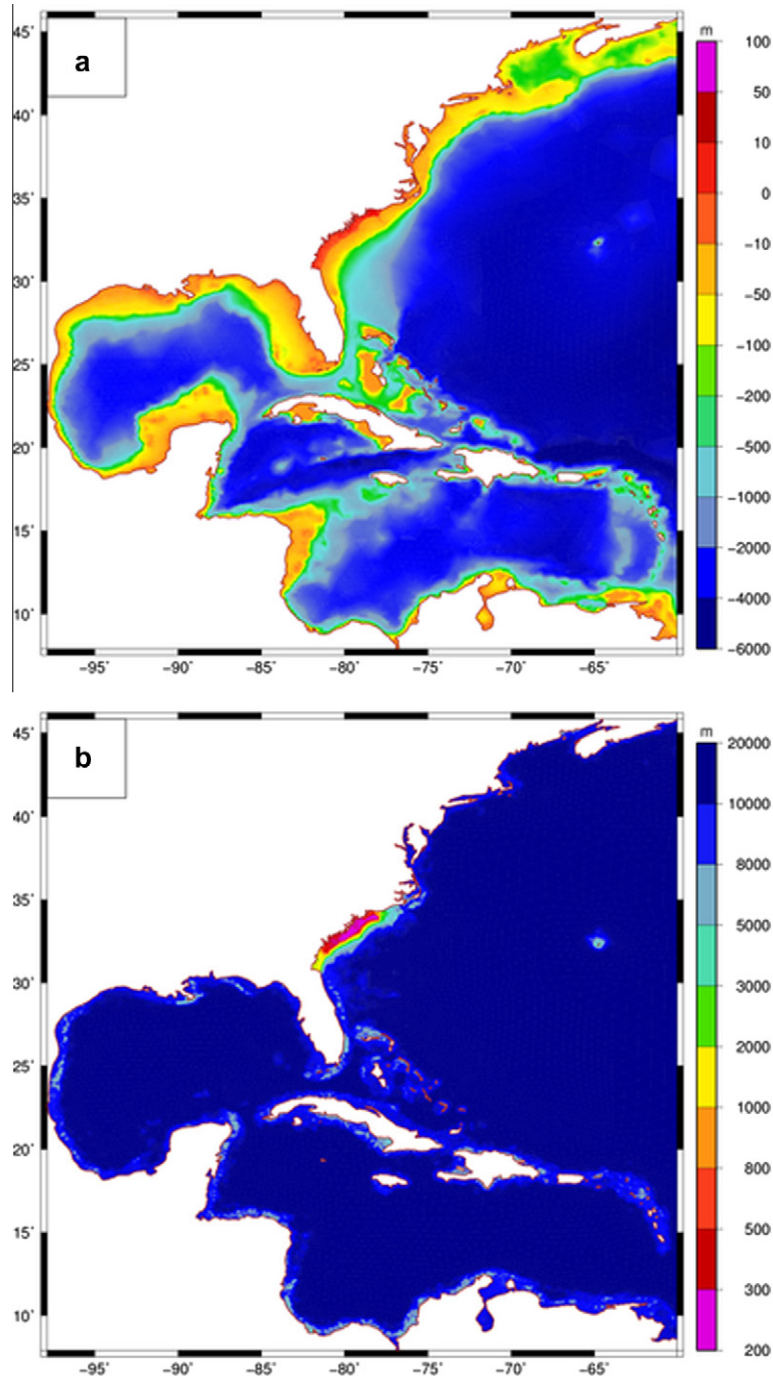


Fig. 14. The SC12 mesh, with panels of (a) bathymetry (m) relative to NAVD 88 (2004.65), and (b) unstructured mesh resolution (m).

4. Conclusions

This work proposes and evaluates CFL-based limiters for the spectral propagation velocities in SWAN. These limiters prevent the excessive directional turning and frequency shifting that can occur on coarsely-resolved computational meshes. On a simplified test case on regular meshes without source terms or ambient currents, the limiter was shown to prevent waves from refracting prematurely over a circular shoal on a coarse mesh, and it also did not harm the computed solution when employed on a fine mesh with sufficient resolution to capture the refraction process.

In test cases in deep water, excessive directional turning can focus energy at a single mesh vertex and create significant wave heights of 150 m or larger. And in test cases in the nearshore, where the significant wave heights are depth-limited, excessive current-induced frequency shifting can push wave energy to the smallest discretized frequency bin and create peak wave periods of 30 s or larger. The limiters were shown to prevent these behaviors. With $\alpha_0 = 0.5$, excessive refraction of swell during a Katrina hindcast was eliminated at locations in the Caribbean Sea and the Atlantic Ocean. And, with $\alpha_0 = \alpha_\sigma = 0.25$, excessive directional turning and frequency shifting of swell and wind-waves during a

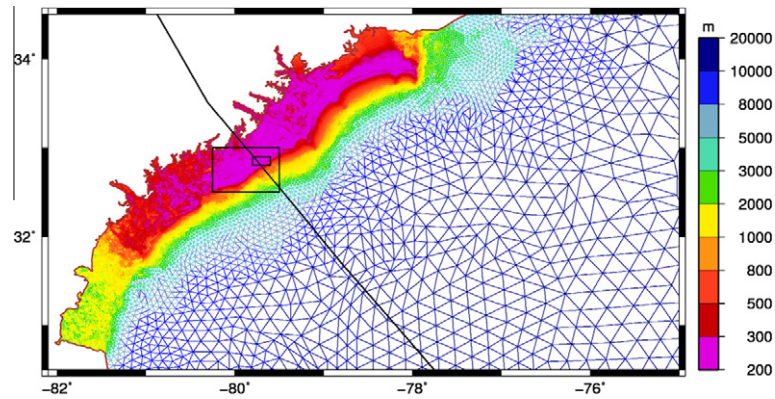


Fig. 15. Unstructured mesh resolution (m) in the region near South Carolina in the SC12 mesh. Black boxes indicate the extents of the zooms shown in Figs. 16,17. The hurricane track is also indicated.

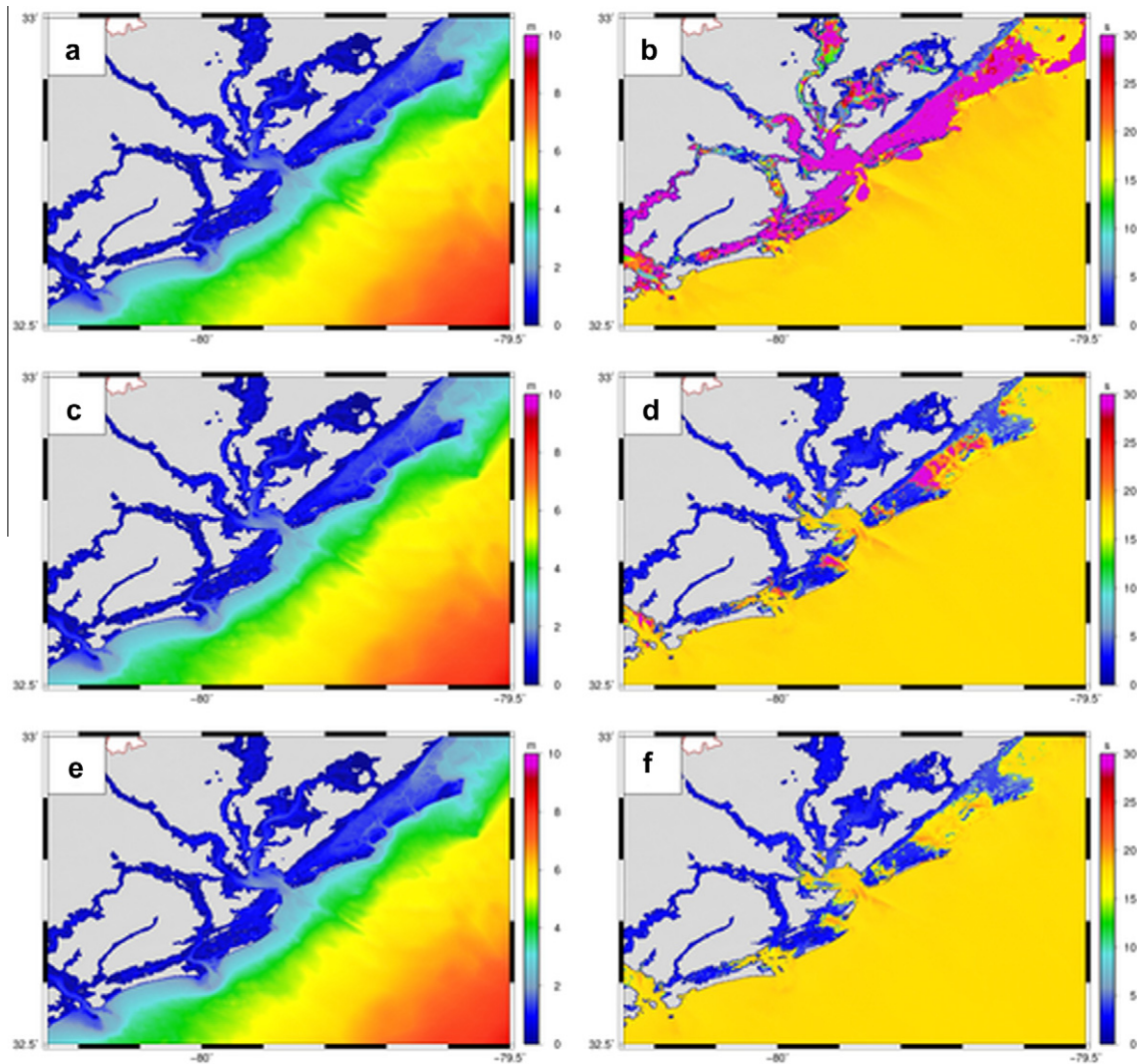


Fig. 16. Maximum values for significant wave heights (m) and peak wave periods (s) near Charleston Harbor during the Hugo hindcast on the SC12 mesh. The significant heights are shown in the left column in panels (a), (c) and (e); and the peak periods are shown in the right column in panels (b), (d) and (f). The top row of panels (a) and (b) are results with unlimited spectral propagation velocities; the middle row of panels (c) and (d) are results with the turning rate limited with $\alpha_\theta = 0.25$; and the bottom row of panels (e) and (f) are results with both velocities limited with $\alpha_\theta = \alpha_\sigma = 0.25$.

Hugo hindcast was controlled at locations along the coastline of South Carolina.

The results herein support the selection of limiters in the range of 0.25 to 0.5, but the proper selection of the limiters is

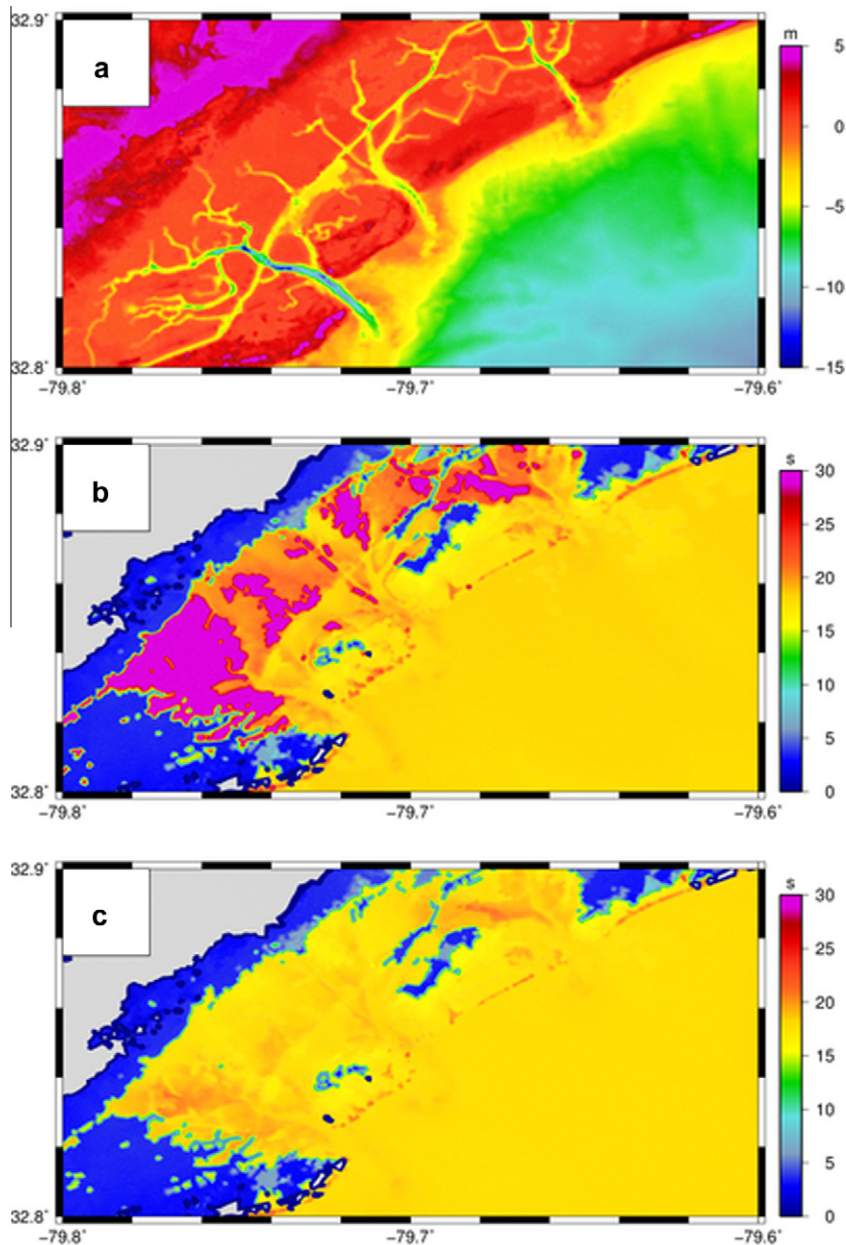


Fig. 17. Details of the Hugo hindcast near Isle of Palms, South Carolina, with panels of: (a) bathymetry (m) in the SC12 mesh; (b) maximum peak wave periods (s) with the turning rate limited with $\alpha_\theta = 0.25$; and (c) maximum peak wave periods (s) with both velocities limited with $\alpha_\theta = \alpha_\sigma = 0.25$.

application-dependent. If the limiters are utilized, then the modeler is advised to select values as large as possible, to control the largest accuracy errors without too much restriction on the wave propagation. Some applications may allow for limiters larger than unity, for instance.

When the available computing resources do not allow for the highest levels of mesh resolution, the limiters can control the largest accuracy errors due to directional turning and/or frequency shifting in under-resolved regions. However, it is emphasized that the limiters do not eliminate these errors, and thus they are not a replacement for finer mesh resolution. The optimal discretization will permit c_θ and c_σ to attain the large values required by the physical situation (as in the presence of steep bottom slopes or strong current gradients). This careful discretization can be achieved by either increasing the spectral resolution (increase $\Delta\theta$ and/or $\Delta\sigma$) and/or decreasing the geographic resolution (decrease Δx and Δy). However, the former option seems hypothetical as it

is restricted by the need to resolve the spectrum and by the tuning conditions of the discrete interaction approximation. Refining the geographic resolution is therefore the preferred option.

Acknowledgements

This work was supported with funding from the National Science Foundation (DMS-0915223). The realistic wind fields for the Katrina and Hugo applications were developed by OceanWeather, Inc. The South Carolina Department of Natural Resources (SCDNR) provided access to the mesh and storm files applied for the South Carolina coastal analysis.

Appendix A

The propagation velocities in spectral space are defined as (Whitham, 1974; Phillips, 1977; Mei, 1983):

$$c_\sigma = \frac{\partial \sigma}{\partial H} \left(\frac{\partial H}{\partial t} + \vec{u} \cdot \nabla_x H \right) - c_g \vec{k} \cdot \frac{\partial \vec{u}}{\partial s} \quad (A1)$$

and:

$$c_\theta = -\frac{1}{|\vec{k}|} \left(\frac{\partial \sigma}{\partial H} \frac{\partial H}{\partial m} + \vec{k} \cdot \frac{\partial \vec{u}}{\partial m} \right) \quad (A2)$$

where (s, m) are left-turning spatial coordinates chosen so that s is in the wave direction θ and m is perpendicular, $\vec{k} = (|\vec{k}| \cos \theta, |\vec{k}| \sin \theta)$ is the wave number vector, H is the total water depth, c_g is the group velocity, and $\vec{u} = (u_x, u_y)$ are the ambient currents.

An expression for $\partial \sigma / \partial H$ can be obtained through differentiation of the dispersion relationship to obtain:

$$\frac{\partial \sigma}{\partial H} = \frac{|\vec{k}| \sigma}{\sinh(2|\vec{k}|H)}$$

With this substitution in Eqs. (A1), (A2), the propagation velocities can be converted from the (s, m) system to Cartesian coordinates (x, y) as follows:

$$c_\sigma = \frac{|\vec{k}| \sigma}{\sinh(2|\vec{k}|H)} \left(\frac{\partial H}{\partial t} + u_x \frac{\partial H}{\partial x} + u_y \frac{\partial H}{\partial y} \right) - c_g |\vec{k}| \left(\frac{\partial u_x}{\partial x} \cos^2 \theta + \frac{\partial u_x}{\partial y} \cos \theta \sin \theta + \frac{\partial u_y}{\partial x} \sin \theta \cos \theta + \frac{\partial u_y}{\partial y} \sin^2 \theta \right) \quad (A3)$$

and:

$$c_\theta = \frac{\sigma}{\sinh(2|\vec{k}|H)} \left(\frac{\partial H}{\partial x} \sin \theta - \frac{\partial H}{\partial y} \cos \theta \right) + \frac{\partial u_x}{\partial x} \cos \theta \sin \theta - \frac{\partial u_x}{\partial y} \cos^2 \theta + \frac{\partial u_y}{\partial x} \sin^2 \theta - \frac{\partial u_y}{\partial y} \sin \theta \cos \theta. \quad (A4)$$

Finally, Eqs. (A3), (A4) can be converted to spherical coordinates (with longitudes λ and latitudes φ in degrees) by using the following relations:

$$dx = R \cos \varphi d\lambda, \quad dy = R d\varphi$$

where R is the radius of the earth. Substitution yields:

$$c_\sigma = \frac{|\vec{k}| \sigma}{\sinh(2|\vec{k}|H)} \left(\frac{\partial H}{\partial t} + \frac{u_x}{R \cos \varphi} \frac{\partial H}{\partial \lambda} + \frac{u_\varphi}{R} \frac{\partial H}{\partial \varphi} \right) - \frac{c_g |\vec{k}|}{R} \left(\frac{1}{\cos \varphi} \frac{\partial u_x}{\partial \lambda} \cos^2 \theta + \frac{\partial u_x}{\partial \varphi} \cos \theta \sin \theta + \frac{1}{\cos \varphi} \frac{\partial u_\varphi}{\partial \lambda} \sin \theta \cos \theta + \frac{\partial u_\varphi}{\partial \varphi} \sin^2 \theta \right) \quad (A5)$$

and:

$$c_\theta = \frac{\sigma}{R \sinh(2|\vec{k}|H)} \left(\frac{1}{\cos \varphi} \frac{\partial H}{\partial \lambda} \sin \theta - \frac{\partial H}{\partial \varphi} \cos \theta \right) + \frac{1}{R} \left(\frac{1}{\cos \varphi} \frac{\partial u_x}{\partial \lambda} \cos \theta \sin \theta - \frac{\partial u_x}{\partial \varphi} \cos^2 \theta + \frac{1}{\cos \varphi} \frac{\partial u_\varphi}{\partial \lambda} \sin^2 \theta - \frac{\partial u_\varphi}{\partial \varphi} \sin \theta \cos \theta \right) \quad (A6)$$

where $\vec{u} = (u_x, u_\varphi)$ are the ambient currents in geographic space. However, the expression for c_θ in Eq. (A6) does not account for the change of propagation direction relative to true north when traveling along a great circle. Clairaut's equation:

$$R \cos \varphi \cos \theta = C$$

where C is a constant, is differentiated with respect to the coordinate s in the wave direction θ to obtain:

$$-R \sin \varphi \cos \theta \frac{d\varphi}{ds} - R \cos \varphi \sin \theta \frac{d\theta}{ds} = 0.$$

With the following substitutions:

$$\frac{d\varphi}{ds} = \frac{1}{R} \sin \theta, \quad \frac{d\theta}{dt} = \frac{d\theta}{ds} \frac{ds}{dt} = \frac{d\theta}{ds} (c_\lambda \cos \theta + c_\varphi \sin \theta)$$

the following expression can be written for $d\theta/dt$:

$$\frac{d\theta}{dt} = - \left(\frac{c_\lambda \cos \theta + c_\varphi \sin \theta}{R} \right) \cos \theta \tan \varphi$$

where $(c_\lambda, c_\varphi) = \vec{c}_g + \vec{u}$ is the geographic propagation velocity. This expression also holds for deep water and the absence of currents, so it can be added to the turning rate c_θ , and the Eqs. (A5), (A6) become:

$$c_\sigma = \frac{|\vec{k}| \sigma}{\sinh(2|\vec{k}|H)} \left(\frac{\partial H}{\partial t} + \frac{u_x}{R \cos \varphi} \frac{\partial H}{\partial \lambda} + \frac{u_\varphi}{R} \frac{\partial H}{\partial \varphi} \right) - \frac{c_g |\vec{k}|}{R} \left(\frac{1}{\cos \varphi} \frac{\partial u_x}{\partial \lambda} \cos^2 \theta + \frac{\partial u_x}{\partial \varphi} \cos \theta \sin \theta + \frac{1}{\cos \varphi} \frac{\partial u_\varphi}{\partial \lambda} \sin \theta \cos \theta + \frac{\partial u_\varphi}{\partial \varphi} \sin^2 \theta \right) \quad (A7)$$

and:

$$c_\theta = \frac{\sigma}{R \sinh(2|\vec{k}|H)} \left(\frac{1}{\cos \varphi} \frac{\partial H}{\partial \lambda} \sin \theta - \frac{\partial H}{\partial \varphi} \cos \theta \right) + \frac{1}{R} \left(\frac{1}{\cos \varphi} \frac{\partial u_x}{\partial \lambda} \cos \theta \sin \theta - \frac{\partial u_x}{\partial \varphi} \cos^2 \theta + \frac{1}{\cos \varphi} \frac{\partial u_\varphi}{\partial \lambda} \sin^2 \theta - \frac{\partial u_\varphi}{\partial \varphi} \sin \theta \cos \theta \right) - \left(\frac{c_\lambda \cos \theta + c_\varphi \sin \theta}{R} \right) \cos \theta \tan \varphi \quad (A8)$$

which are the spectral propagation velocities expressed in spherical coordinates with longitudes λ and latitudes φ .

References

- Amante, C., Eakins, B.W., 2009. ETOPO1 1 Arc-minute global relief model: procedures, data sources and analysis. NOAA Technical Memorandum NESDIS NGDC-24, pp. 19.
- Babanin, A.V., Hsu, T.-W., Roland, A., Ou, S.-H., Doong, D.-J., Kao, C.C., 2011. Spectral wave modelling of Typhoon Krosa. Nat. Hazards Earth Syst. Sci. 11, 501–511.
- Battjes, J.A., Janssen, J.P.F.M., 1978. Energy loss and set-up due to breaking of random waves. In: Proceedings of the 16th International Conference on Coastal Engineering, ASCE, pp. 569–587.
- Bennis, A.-C., Arduhin, F., Dumas, F., 2011. On the coupling of wave and three-dimensional circulation models: choice of theoretical framework, practical implementation and adiabatic tests. Ocean Modell. 40, 260–272.
- Bertotti, L., Cavaleri, L., 2012. Modelling waves at Orkney coastal locations. J. Marine Syst. 96–97, 116–121.
- Booij, N., Holthuijsen, L.H., 1987. Propagation of ocean waves in discrete spectral wave models. J. Comput. Phys. 68, 307–326.
- Booij, N., Ris, R.C., Holthuijsen, L.H., 1999. A third-generation wave model for coastal regions. Part I, Model description and validation. J. Geophys. Res. 104, 7649–7666.
- Bretschneider, C.L., Krock, H.J., Nakazaki, E., Casciano, F.M., 1986. Roughness of typical Hawaiian terrain for tsunami runup calculations: a users manual. J.K.K. Look Laboratory Report, University of Hawaii, pp. 42.
- Brown, J.M., 2010. A comparison of WAM and SWAN under storm conditions in a shallow water application. Ocean Modell. 35 (3), 215–229.
- Brown, J.M., Bolanos, R., Wolf, J., 2011. Impact assessment of advanced coupling features in a tide-surge-wave model, POLCOMS-WAM, in a shallow water application. J. Marine Syst. 87, 13–24.
- Bunya, S., Dietrich, J.C., Westerink, J.J., Ebersole, B.A., Smith, J.M., Atkinson, J.H., Jensen, R.E., Resio, D.T., Luettich Jr., R.A., Dawson, C.N., Cardone, V.J., Cox, A.T., Powell, M.D., Westerink, H.J., Roberts, H.J., 2010. A high resolution coupled riverine flow, tide, wind, windwave and storm surge model for Southern Louisiana and Mississippi: Part I – Model development and validation. Mon. Weather Rev. 138 (2), 345–377.
- Cardone, V.J., Cox, A.T., 2009. Tropical cyclone wind forcing for surge models: critical issues and sensitivities. Natural Hazards 51, 29–47.
- Cavaleri, L., Malanotte-Rizzoli, P., 1981. Wind wave prediction in shallow water: theory and applications. J. Geophys. Res. 86 (C11), 10961–10973.
- Cox, A.T., Greenwood, J.A., Cardone, V.J., Swail, V.R., 1995. An interactive objective kinematic analysis system. In: Fourth International Workshop on Wave Hindcasting and Forecasting, Banff, Alberta, Canada, Atmospheric Environment Service, pp. 109–118.
- Dawson, C.N., Westerink, J.J., Feyen, J.C., Pothina, D., 2006. Continuous, discontinuous and coupled discontinuous-continuous Galerkin finite element methods for the shallow water equations. Int. J. Numer. Methods Fluids 52, 63–88.
- Dietrich, J.C., Bunya, S., Westerink, J.J., Ebersole, B.A., Smith, J.M., Atkinson, J.H., Jensen, R.E., Resio, D.T., Luettich Jr., R.A., Dawson, C.N., Cardone, V.J., Cox, A.T., Powell, M.D., Westerink, H.J., Roberts, H.J., 2010. A high resolution coupled riverine flow, tide, wind, wind wave and storm surge model for Southern Louisiana and Mississippi: Part II – synoptic description and analyses of hurricanes Katrina and Rita. Mon. Weather Rev. 138, 378–404.

- Dietrich, J.C., Zijlema, M., Westerink, J.J., Holthuijsen, L.H., Dawson, C.N., Luettich Jr., R.A., Jensen, R.E., Smith, J.M., Stelling, G.S., Stone, G.W., 2011a. Modeling hurricane waves and storm surge using integrally-coupled, scalable computations. *Coast. Eng.* 58, 45–65.
- Dietrich, J.C., Westerink, J.J., Kennedy, A.B., Smith, J.M., Jensen, R.E., Zijlema, M., Holthuijsen, L.H., Dawson, C.N., Luettich Jr., R.A., Powell, M.D., Cardone, V.J., Cox, A.T., Stone, G.W., Pourtaheri, H., Hope, M.E., Tanaka, S., Westerink, L.G., Westerink, H.J., Cobell, Z., 2011b. Hurricane Gustav (2008) waves and storm surge: hindcast, validation and synoptic analysis in Southern Louisiana. *Mon. Weather Rev.* 139 (8), 2488–2522.
- Dietrich, J.C., Tanaka, S., Westerink, J.J., Dawson, C.N., Luettich Jr., R.A., Zijlema, M., Holthuijsen, L.H., Smith, J.M., Westerink, L.G., Westerink, H.J., 2012. Performance of the unstructured-mesh, SWAN+ADCIRC model in computing hurricane waves and surge. *J. Sci. Comput.* 52 (2), 468–497. <http://dx.doi.org/10.1007/s10915-011-9555-6>.
- Ebersole, B.A., Westerink, J.J., Resio, D.T., Dean, R.G., 2007. Performance evaluation of the New Orleans and Southeast Louisiana hurricane protection system. vol. IV – The storm. Final report of the interagency performance evaluation task force, U.S. Army Corps of Engineers, Washington, DC.
- Ebersole, B.A., Westerink, J.J., Bunya, S., Dietrich, J.C., Cialone, M.A., 2010. Development of storm surge which led to flooding in St. Bernard Polder during Hurricane Katrina. *Ocean Eng.* 37, 91–103.
- Federal Emergency Management Agency (FEMA), 2009. Flood insurance study: Southeastern Parishes, Louisiana, intermediate submission 2: offshore water levels and waves, US Army Corps of Engineers, New Orleans District.
- Federal Emergency Management Agency (FEMA), 2012. South Carolina storm surge project deliverable 2: JPM-OS analysis and storm validation report. April 2012.
- Ferziger, J.H., Peric, M., 1999. *Computational Methods for Fluid Dynamics*, Springer-Verlag, Berlin.
- Hasselmann, S., Hasselmann, K., Allender, J.H., Barnett, T.P., 1985. Computations and parameterizations of the nonlinear energy transfer in a gravity wave spectrum, Part II: Parameterizations of the nonlinear transfer for application in wave models. *J. Phys. Oceanograph.* 15 (11), 1378–1391.
- Holthuijsen, L.H., Herman, A., Booij, N., 2003. Phase-decoupled refraction-diffraction for spectral wave models. *Coast. Eng.* 49, 291–305.
- Hsu, T.W., Ou, S.H., Liao, J.M., 2005. Hindcasting nearshore wind waves using a FEM code for SWAN. *Coast. Eng.* 52 (2), 177–195.
- Kim, K.O., Yamashita, T., 2008. Storm surge simulation using wind-wave-surge coupling model. *J. Oceanograph.* 64, 621–630.
- Knabb, R.D., Rhome, J.R., Brown, D.P., 2005. Tropical Cyclone Report, Hurricane Katrina, 23–30 August. NOAA National Hurricane Center, pp. 43.
- Kolar, R.L., Westerink, J.J., Cantekin, M.E., Blain, C.A., 1994. Aspects of nonlinear simulations using shallow water models based on the wave continuity equations. *Comput. Fluids* 23, 523–538.
- Komen, G.J., Hasselmann, S., Hasselmann, K., 1984. On the existence of a fully developed wind-sea spectrum. *J. Phys. Oceanogr.* 14, 1271–1285.
- Komen, G., Cavaleri, L., Donelan, M., Hasselmann, K., Hasselmann, S., Janssen, P.A.E.M., 1994. *Dynamics and Modeling of Ocean Waves*. Cambridge University Press, Cambridge.
- Liu, H., Xie, L., 2009. A numerical study on the effects of wavecurrentsurge interactions on the height and propagation of sea surface waves in Charleston Harbor during Hurricane Hugo 1989. *Cont. Shelf Res.* 29, 1454–1463.
- Luettich, R.A., Westerink, J.J., 2004. Formulation and numerical implementation of the 2D/3D ADCIRC finite element model version 44.XX, pp. 74. <http://adcirc.org/adcirctheory20041208.pdf>.
- Madsen, O.S., Poon, Y.-K., Graber, H.C., 1988. Spectral wave attenuation by bottom friction: theory. In: *Proceedings 21st International Conference on Coastal Engineering*, ASCE, pp. 492–504.
- Mei, C.C., 1983. *The Applied Dynamics of Ocean Surface Waves*. Wiley, New York, p. 740.
- Mukai A.Y., Westerink, J.J., Luettich Jr., R.A., Mark, D., 2002. Eastcoast 2001: a tidal constituent database for the western North Atlantic, Gulf of Mexico and Caribbean Sea. US Army Engineer Research and Development Center, Coastal and Hydraulics Laboratory, Technical Report, ERDC/CHL TR-02-24, September 2002, p. 201.
- Peng, M., Xie, L., Pietrafesa, L.J., 2006. A numerical study on hurricane-induced storm surge and inundation in Charleston Harbor, South Carolina. *J. Geophys. Res.* 111, C08017. <http://dx.doi.org/10.1029/2004JC002755>.
- Phillips, O.M., 1977. *The Dynamics of the Upper Ocean*. Cambridge University Press, p. 336.
- Powell, M., Houston, S., Reinhold, T., 1996. Hurricane Andrew's landfall in South Florida, Part I: Standardizing measurements for documentation of surface wind fields. *Weather Forecast.* 11, 304–328.
- Powell, M., Houston, S., Morrisseau-Leroy, N., 1998. The HRD real-time hurricane wind analysis system. *J. Wind Eng. Ind. Aerod.* 77–78, 53–64.
- Qi, J., Chen, C., Beardsley, R.C., Perrie, W., Cowles, G.W., Lai, Z., 2009. An unstructured-grid finite-volume surface wave model (FVCOM-SWAVE): implementation, validations and applications. *Ocean Modell.* 28, 153–166.
- Ris, R.C., Booij, N., Holthuijsen, L.H., 1999. A third-generation wave model for coastal regions, Part II. verification. *J. Geophys. Res.* 104, 7667–7681.
- Rogers, W.E., Hwang, P.A., Wang, D.W., 2003. Investigation of wave growth and decay in the SWAN model: three regional-scale applications. *J. Phys. Oceanograph.* 33, 366–389.
- Rogers, W.E., Kaihatu, J.M., Hsu, L., Jensen, R.E., Dykes, J.D., Holland, K.T., 2007. Forecasting and hindcasting waves with the SWAN model in the Southern California Bight. *Coastal Eng.* 54, 1–15.
- Roland, A., 2009. Development of the WWMII: spectral wave modeling on unstructured meshes. Ph.D. thesis, Institute for Hydraulic and Water Resources Engineering, University of Technology Darmstadt.
- Smith, J.M., Sherlock, A.R., Resio, D.T., 2001. STWAVE: Steady-state spectral wave model user's manual for STWAVE, Version 3.0. USACE, Engineer Research and Development Center. Technical Report ERDC/CHL SR-01-1, Vicksburg, MS.
- Snyder, R.L., Dobson, F.W., Elliott, J.A., Long, R.B., 1981. Array measurements of atmospheric pressure fluctuations above surface gravity waves. *J. Fluid Mech.* 102, 1–59.
- Stelling, G.S., Leendertse, J.J., 1992. Approximation of convective processes by cyclic AOI methods. In: *Proceedings of the 2nd International Conference on Estuarine and coastal modeling*, ASCE Tampa, Florida, 771–782.
- Tolman, H.L., 2009. User manual and system documentation of WAVEWATCH III version 3.14. NOAA/NWS/NCEP/MMAB Technical Note 276, <http://polar.ncep.noaa.gov/mmap/papers/tm276/MMAB276.pdf>.
- USACE, 2009. Hydraulics and hydrology appendix, Louisiana coastal protection and restoration: Final Technical Report, US Army Engineer District, New Orleans, LA, pp. 389.
- WAMDI Group, 1988. The WAM model: a third generation ocean wave prediction model. *J. Phys. Oceanograph.* 18 1775–1810.
- Wang, D.P., Oey, L.Y., 2008. Hindcast of waves and currents in Hurricane Katrina. *B. Am. Meteorol. Soc.* 89 (4), 487–495.
- Westerink, J.J., Coauthors, 2008. A basin- to channel-scale unstructured grid hurricane storm surge model applied to Southern Louisiana. *Mon. Weather Rev.* 136, 833–864.
- Whitham, G.B., 1974. *Linear and Nonlinear Waves*. Wiley, New York, p. 636.
- Xie, L., Liu, H., Peng, M., 2008. The effect of wave-current interactions on the storm surge and inundation in Charleston Harbor during Hurricane Hugo 1989. *Ocean Modell.* 20, 252–269.
- Zijlema, M., 2010. Computation of wind-wave spectra in coastal waters with SWAN on unstructured grids. *Coastal Eng.* 57, 267–277.
- Zijlema, M., van der Westhuysen, A.J., 2005. On convergence behaviour and numerical accuracy in stationary SWAN simulations of nearshore wind-wave spectra. *Coastal Eng.* 52 (3), 237–256.